Discover Nano

Research

Viscoelastic modelling and analysis of two-dimensional woven CNT-based multiscale fibre reinforced composite material system

Ashirbad Swain[1] · Vignesh Palani[1] · Sigil Francis[1] · Benedict Thomas[1] · Tarapada Roy[2]

Received: 14 September 2023 / Accepted: 9 April 2024
Published online: 30 April 2024
© The Author(s) 2024 OPEN

Abstract
Carbon nanotube (CNT) has fostered research as a promising nanomaterial for a variety of applications due to its exceptional mechanical, optical, and electrical characteristics. The present article proposes a novel and comprehensive micromechanical framework to assess the viscoelastic properties of a multiscale CNT-reinforced two-dimensional (2D) woven hybrid composite. It also focuses on demonstrating the utilisation of the proposed micromechanics in the dynamic analysis of shell structure. First, the detailed constructional attributes of the proposed trans-scale composite material system are described in detail. Then, according to the nature of the constructional feature, mathematical modelling of each constituent phase or building block's material properties is established to evaluate the homogenised viscoelastic properties of the proposed composite material system. To highlight the novelty of this study, the viscoelastic characteristics of the modified matrix are developed using the micromechanics method of Mori–Tanaka (MT) in combination with the weak viscoelastic interphase (WI) theory. In the entire micromechanical framework, the CNTs are considered to be randomly oriented. The strength of the material (SOM) approach is used to establish mathematical frameworks for the viscoelastic characteristics of yarns, whereas the unit cell method (UCM) is used to determine the viscoelastic properties of the representative unit cell (RUC). Different numerical results have been obtained by varying the CNT composition, interface conditions, agglomeration, carbon fibre volume percentage, excitation frequency, and temperature. The influences of geometrical parameters like yarn thickness, width, and the gap length to yarn width ratio on the viscoelasticity of such composite material systems are also explored. The current study also addresses the issue of resultant anisotropic viscoelastic properties due to the use of dissimilar yarn thickness. The results of this micromechanical analysis provide valuable insights into the viscoelastic properties of the proposed composite material system and suggest its potential applications in vibration damping. To demonstrate the application of developed novel micromechanics in vibration analysis, as one of the main contributions, comprehensive numerical experiments are conducted on a shell panel. The results show a significant reduction in vibration amplitudes compared to traditional composite materials in the frequency response and transient response analyses. To focus on the aspect of micromechanical behaviour on dynamic response and for the purpose of brevity, only linear strain displacement relationships are considered for dynamic analysis. These insights could inform future research and development in the field of composite materials.

Keywords CNTs · Conventional carbon fibres · CNTs based woven fabric composite · Mori–Tanaka micromechanics · Weak viscoelastic interphase · Unit cell method · Strength of material method · Viscoelastic properties

✉ Ashirbad Swain, ashirbad.swain@vit.ac.in; ashi.jpub@gmail.com | [1]School of Mechanical Engineering, Vellore Institute of Technology, Vellore, Tamil Nadu 632014, India. [2]Department of Mechanical Engineering, National Institute of Technology, Rourkela, Odisha 769008, India.

List of symbols

CNT	Carbon-nanotube
2D	2-Dimensional
MT	Mori-Tanaka
WI	Weak viscoelastic interphase
SOM	Strength of materials
UCM	Unit cell method
RUC	Representative unit cell
NC	Nano-composite
pf	Packing factor
RVE	Representative volume element
MWCNT	Multi-walled carbon-nanotube
CFRP	Carbon fiber reinforced polymer
GA	Genetic algorithm
σ^P	Stress of matrix phase
$\dot{\varepsilon}^P$	Strain rate of matrix phase
C^P	Stiffness of matrix phase
$E^P_\infty, E^P_j, \tau^P_i$	Coefficients of the Prony series
$\overline{\sigma}^{NC}$	Average state of stresses in the configuration of 'a'
$\overline{\sigma}^{P}$	Average state of stresses in the configuration of 'b'
ε^*	Eigen-strain
S	Eshelby's tensor
S^P	Compliance tensor for polymer material
I	Fourth order identity tensor
ε_a	Average strain
v^P_{NC}	Volume fractions of matrix
v^{CNT}_{NC}	Volume fractions of CNTs
A^{ndil}	Non-dilute strain concentration tensor
S_I	Interface
n	Unit vector normal to S_I
$u_i(S_I^+)$	Displacements when approached from inside of the inclusion
$u_i(S_I^-)$	Displacements when approached from outside of the inclusion
V^{CNT}_{NC}	Total volume of CNTs
$V^{CNT}_{Cluster}$	CNTs trapped inside the cluster
V^{CNT}_{P}	Remaining CNT in the polymer phase outside the cluster
ξ	Volume fraction of the spherical cluster with respect to the RVE
d_{cnt}	Diameter of CNTs
l_{cnt}	Length of CNTs
α	Interfacial compliance
α'	Real part of interfacial compliance
α''	Imaginary part of interfacial compliance
α''/α'	Interfacial loss factor
α_0	Non-dimensional interfacial compliance
v_F	Volume fractions of carbon fibres
v_{NC}	Volume fractions of modified matrix
r_f, r_w	Radius of curvature of fill and warp yarn
t_f, t_w	Thickness of fill and warp yarn
S_{Ff}, S_{Fw}	Shape factor of fill and warp yarn
$S_{Ff}t_f, S_{Fw}t_w$	Width of fill and warp yarn
β_{cf} and β_{cw}	Crimp angles corresponding to fill and warp yarn

1 Introduction

Woven fabric composites have been employed in a wide range of engineering applications. In woven composites, when a strand breaks in the weave, the load is carried by the surrounding fibres. However, in unidirectional composites, fibre breakage or puncture can affect strength over the entire length of the fibre. As a result, woven fabric composites have been a popular research topic for decades. Woven fabric in the composite material system offers improved overall strength and stiffness characteristics in all directions due to fibre undulation and orientation of undulated fibres aligned a minimum of two axes. To assess the elastic properties of woven composites, several micromechanical models have been presented. Here are a few of the critical articles in this field.

Ishikawa and Chou [1] introduced the undulation, mosaic, and bridging models, which can be used as a basic model for 2D woven fabric composites. Yang et al. [2] proposed a fibre inclination model (i.e., fibre undulation model) in which actual elastic parameters were found utilising a traditional lamination theory-based iso-stress condition approach. Zhang and Harding [3] use the strain energy equivalence theory and the finite element method for the micromechanical analysis of the plain weave composite. A two-dimensional woven fabric (2D-WF) model was developed by Naik and Ganesh [4]. Similar research work was presented by Shembekar and Naik [5] and Ganesh and Naik [6, 7], which was helpful for the prediction of in-plane elastic moduli. The combi-cell model by Vandeurzen et al. [8, 9] can evaluate the shear modulus correctly. Scida et al. [10] developed the MESOTEX model, which used multiple functions to describe fibre geometry and determine the elastic characteristics of woven hybrid composites. Barbero et al. [11] proposed a periodic microstructure model to assess the elasticity of plane wave composites, whereas Barbero et al. [12] reported a comparison between the periodic microstructure model and the finite element model in their research. Donadon et al. [13] established a model for calculating the elastic characteristics of plane weave composites in the warp and weft directions, taking into consideration various undulations and material parameters. They pointed out some inconsistencies in Shembekar and Naik's model [14] in their research. Barbero [15] and Adumitroaie and Barbero [16] suggested a simple bending restrained model that only required a quarter of a typical unit cell to calculate the thermoelastic properties of a 2D woven fabric composite. In order to analyze the elastic behaviour of 2D plane weave composites, Kowalczyk [17] suggested a typical homogenization technique based on finite elements, which used a periodic-repeated volume element in their modelling techniques. Shokrieh et al. [18] proposed a generalized multiscale micromechanical model to predict the strength and elastic properties of 2D plane weave composites based on the laminate analogy method, in which the entire representative unit cell is divided into sub-domains, and elastic properties are obtained for each domain. Wang et al. [19] used systematic studies to investigate the effects of temperature and strain rate on the stress–strain behaviours of plain and 4-harness satin woven fibre reinforced composites and proposed a constitutive model that accounted for damage progression. Hwang et al. [20] used a genetic algorithm (GA) to improve the elastic modulus of woven fabric composites based on the micromechanics and the geometric modelling presented by Scida et al. [10, 21, 22]

There is very little literature for woven composites when viscoelasticity thermomechanical effects are taken into account. Govindarajan et al. [23] investigated the creep response of woven composites using both experimental and analytical methods. The authors used the correspondence principle and the Maxell-Voigt four-element model to predict the viscoelastic behaviour of the matrix material in their mathematical formulations, which were built on the work of Ishikawa and Chou [24]. Zhu et al. [25] presented and compared a three-dimensional viscoelastic model to estimate time-dependent viscoelastic creep compliance. The relationship between the relaxation property of the matrix material and the time-dependent flexural properties of the fibre bundle was demonstrated in this work. By considering the viscoelastic property of the polyimide matrix, Rupnowski and Kumosa [26] performed a finite element-based stress analysis of eight harness satin/polyimide matrix composites to determine residual stress in a woven composite. Shrotriya and Sottos [27] used dynamic mechanical analysis to investigate the creep responses of woven composites for multilayer printed circuit boards, measuring creep compliance in the warp and fill directions. [21].

Shrotriya and Sottos [28] devised a micromechanical framework for predicting woven composites' time–temperature dependent material properties for multilayer printed circuit boards. Viscoelastic storage and loss moduli of FR-4 materials utilised in microelectronic devices were determined by Kim [29] using the technique developed by Sottos [30]. The model may predict the relaxation behaviour of the material system in addition to the storage and loss moduli. Greco et al. [31] studied the viscoelastic short term flexural creep response of glass fibre/polypropylene-based woven composites. The linearity of viscoelasticity of the material was examined using Boltzmann's superposition

principle and varied stress levels, with the scientists finding that increased temperature resulted in lesser creep compliance. Using the finite element method and volume averaging of three independent repeated volume elements, Naik et al. [32] examined the viscoelastic creep and relaxation behaviour of fibre-based polymer matrix composites. Upadhyaya and Upadhyay [33] devised a 3-D micromechanical model using classical lamination theory and calculated the Prony series coefficients for a variety of samples with varying fibre volume fractions in order to investigate the viscoelastic reactions of woven cloth composites while taking into account the viscoelastic influence of the matrix phase. Jia et al. [34] used micro/mesoscale repetitive unit cells to investigate orthogonal woven composites' low cycle tensile response based on their elastic/viscoelastic properties and characterized the viscoelastic behaviour of resin materials with nonlinear viscoelastic relationship along with switch rules. According to microscopic observations of the weave geometry, a realistic mesoscale finite element model was proposed by Wang et al. [35] to model the matrix's mechanical behaviours; a combined elastoplastic-damage model was proposed. Chen and Aliabadi [36] proposed a novel micromechanical approach for predicting woven kenaf composites' overall nonlinear response and rate-dependent behaviour by employing a viscoelastic model with time-dependent periodic boundary conditions in an explicit way meshfree method to describe the polymer matrix's behaviour. Bhattacharjee et al. [37] proposed an operator-based-approach to explain the viscoelastic characteristics of woven hybrid composites for structural dynamic analysis. Liu et al. [38] developed a data-driven two-step homogenization multiscale modelling approach to predict the effective heat conductivity of two-dimensional (2D) woven composites based on structural genome mechanics. Wu et al. [39] adopted a recursive technique involving laminate theories, mean-field homogenization, Voigt's rule of mixtures in their study. Bai et al. [40] present a novel micromechanical model based on the minimal total complementary potential energy concept to give a quick and straightforward prediction of the strength of plain weave fabric composites under biaxial strain.

Carbon nanotubes (CNTs) are renowned for their outstanding mechanical characteristics, making them ideal for reinforcing in the polymeric phase [41–46], but relatively little research has been done in the direction of CNTs-reinforced multiscale woven fabric composites. Kim [47] investigated the elastic response of CNTs/carbon fibre/polymer-based multiscale composite materials using numerical and experimental methods. Sadeghi and Pol [48] examined how nanotube content and indenter form affected the tensile and quasi-static punch shear properties of planar woven fibre reinforced composite laminates. Dikshit and Joshi [49] explored the influence of CNTs content on plane woven composite mode-I interlaminar failure, taking into account overall toughening effects from CNTs and fibres. Nam et al. [50] used a multiscale framework to establish the reliability of the Mori–Tanaka based micro-mechanical failure model for radar-absorbing. Swain et al. [51] studied the thermoelastic characteristics of multiscale woven composite materials with radially aligned CNTs and attached with carbon fibre. El Moumen et al. [52] used multiscale homogenization approaches with finite element analysis to predict elastic properties of CNTs based woven fibre reinforced composite and compare them with experimental data. Fantuzzi et al. [53] presented and compared Chamis, Hahn and Halpin–Tsai homogenization technique to predict elastic properties of multiscale woven fabric composites reinforced by carbon nanotubes. Basilisk and Syduzzaman [54] presented an exhaustive review of the different manufacturing processes of CNTs based woven fibre reinforced composites and encapsulated some essential micromechanical techniques for the prediction of thermomechanical and electrical properties of such composites.

Guo et al. [55] investigated the effects of multiwalled carbon nanotubes (MWCNT) content on mechanical characteristics of nanocomposite with photosensitive matrix. Wang et al. [56] developed a mathematical model to study the damped response of a nanocomposite plate with stiffeners reinforced with randomly oriented CNT. Huang et al. [57] investigated buckling and dynamics response for graphene-reinforced composites, considering the non-local theory. Li et al. [58] and Al-Furjan et al. [59, 60] conducted similar studies based on the non-local stress–strain gradient theorem. Shen et al. [61] developed the governing differential equations considering modified couple stress theory for dynamic analysis of composite reinforced with graphene nanoplatelets. Researchers derived the governing deferral equation employing the Hamilton principle [62–64] for dynamic analysis of graphene nanoplatelet-reinforced composite. Dai et al. [65] considered a non-polynomial viscoelastic model for the dynamic analysis of open-type composite shells under residual stresses.

Based on a review of the literature, it's evident that further work is needed to develop a complete mathematical framework for analysing the frequency and temperature-dependent viscoelastic characteristics of CNTs-based multiscale 2D woven composites. The study's primary aim is to propose a unified micromechanical framework to assess the viscoelastic property of a multiscale 2D woven composite reinforced with a randomly oriented carbon nanotube. Apart from this, an attempt was made to address the anisotropic viscoelastic properties arising due to inequal yar thickness. For the sake of completeness, a sincere effort was made to demonstrate the application of the developed micromechanics for the dynamic analysis of structures made of such multiscale composites using the shell finite

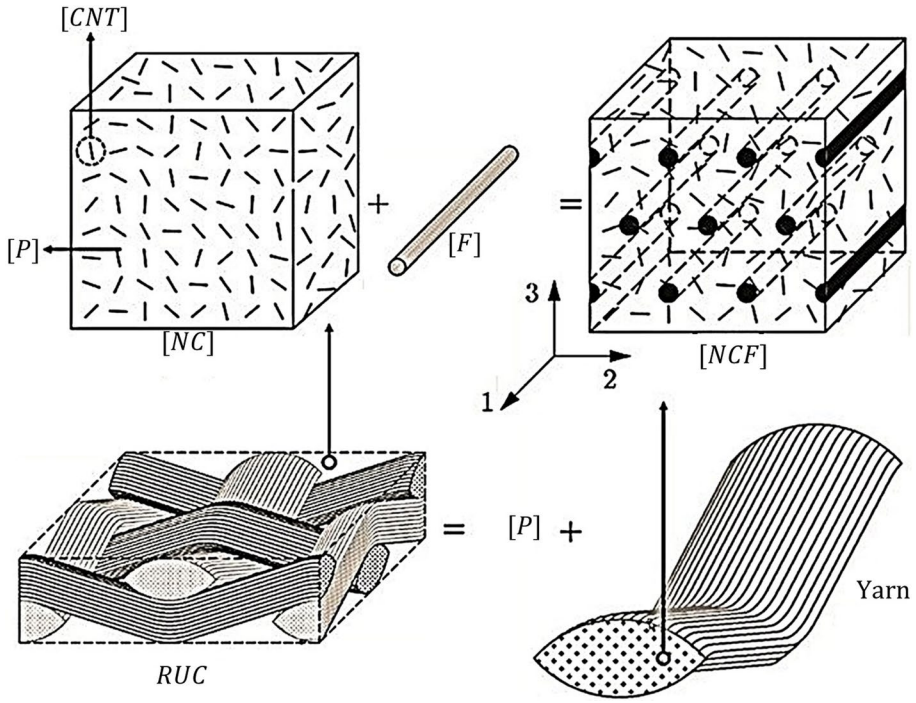

Fig. 1 RUC and the constituents of the proposed Hybrid composite

element method. As a result, the focus of this research is on evaluating the frequency and temperature-dependent viscoelastic characteristics of a two-dimensional woven fabric composite with carbon nanotubes arranged randomly in the polymer phase. First, the Mori–Tanaka micromechanics technique and the viscoelastic weak interphase theory are used to determine the viscoelastic characteristics of nanocomposite. The effect of agglomeration is also taken into account in the micromechanics that have been developed. Following that, in the second mathematical framework, the viscoelastic properties of yarns are formulated using the strength of material method (SOM), and the viscoelastic characteristics of the representative unit cell (RUC) are determined using the unit cell approach (UCM). The elastic properties obtained were compared to those found in the literature for validation. After a two-step validation process, the micromechanics was used to analyse different viscoelastic properties of the proposed composite material system, such as storage moduli (viz. $E_1\prime$, $E_3\prime$, $G_{12}\prime$, and $G_{23}\prime$) and In-pane and out of plane loss factors (viz. η_1, η_3, η_{12}, and η_{23}). The effect of various parameters such as CNTs content, the interphase condition between CNTs and polymer, fibre content, the geometry of and position of yarn in the representative unit cell on the mentioned viscoelastic properties has been investigated considering an eleven-parameter generalized maxwell model. As the proposed material system shows exceptional material damping characteristics, as one of the main contributions, a comprehensive finite element based dynamic analysis was also performed on shell structures to explain the worthiness of the developed micromechanics. For the purpose of brevity, only linear strain displacement relationships are considered for dynamic analysis.

2 Formulation for viscoelastic characteristics of proposed composite

This section describes the constructional features of the proposed nanocomposite hybrid material system and mathematical framework to obtain its viscoelastic properties. Figure 1 depicts the detailed elements of a multiscale material based on carbon fiber/CNTs/polymer and its constituents. It is clear that Carbon nanotubes, carbon fibre, and polymer are the basic building blocks, as seen in Fig. 1. As seen in the figure, the phase [*NC*] results from randomly oriented CNTs in the polymer phase. When the [*NC*] phase is coupled with fibre, it produces a specific portion of yarn. When these yarns are combined with [*NC*], the proposed multiscale composite material is created.

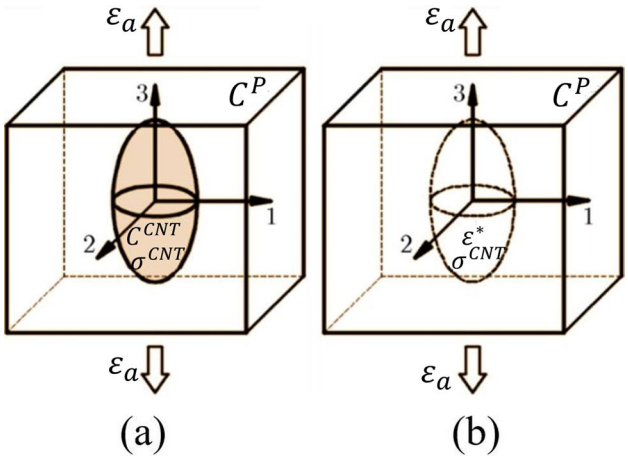

Fig. 2 **a** RVE with inclusion and **b** comparison material without inclusion for Eshelby's Equivalent problem

2.1 The correspondence principle and viscoelasticity

The matrix and CNTs are the two primary phases of the nanocomposite, with the matrix being isotropic and the CNTs being transversely isotropic. Among these two constituent phases, the matrix is viscoelastic. Using the correspondence principle, the constitutive relationship for the viscoelastic matrix phase can be represented as follows [66]:

$$\sigma^P(t) = \int_0^t C^P(t-\Gamma) : \dot{\varepsilon}^P(\Gamma)d\Gamma \tag{1}$$

where σ^P, $\dot{\varepsilon}^P$ and C^P indicate the matrix phase's stress, strain rate, and stiffness, respectively.

In this case, the half-sided Fourier transformation is applied, which is given by

$$\underline{f}(\omega) = \int_0^\infty f(t)e^{-i\omega t}dt \tag{2}$$

As a result, the frequency domain form of the Eq. (1) is as follows:

$$\underline{\sigma}^P(\omega) = i\omega\underline{C}^P(\omega) : \underline{\varepsilon}^P(\omega) \tag{3}$$

The Eq. (3) can alternatively be written in the following way:

$$\underline{\sigma}^P(\omega) = \underline{C}^{P*}(\omega) : \underline{\varepsilon}^P(\omega) \tag{4}$$

The underscore symbol indicates that the parameter is a frequency function rather than a time function, while the star symbol * indicates that the parameter is a complex number. These symbols are not used for brevity because the mechanics hold true in the time and frequency domain.Since the CNT is completely elastic, Hook's law can be represented by fourth-order stiffness tensors C^{CNT}, which can be related to stress and strain as follows.

$$\sigma^{CNT} = C^{CNT} : \varepsilon^{CNT} \tag{5}$$

2.2 Mori–Tanaka micromechanics

Nanocomposite stiffness tensor (i.e., C^{NC}) is evaluated using the MT approach and approximated to be ellipsoidal in the form [67–79]. Figure 2 shows Eshelby's equivalent inclusion problem, with Fig. 2a illustrating the nanocomposite and Fig. 2b illustrating the matrix. In Fig. 2b, the black dotted line represents the volume that the inclusion could occupy.

Average developed stresses in both the domain due to the same average strain (ε_a) caused with a displacement at the boundary

Fig. 3 Illustration of for WI

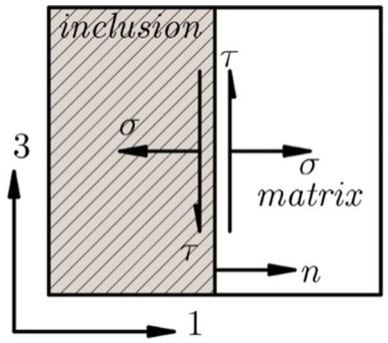

$$\tilde{\sigma}^{NC} = C^{NC} : \varepsilon_a$$
$$\tilde{\sigma}^{P} = C^{P} : \varepsilon_a \tag{6}$$

In the configurations of 'a' and 'b' the average state of stresses are $\tilde{\sigma}^{NC}$ and $\tilde{\sigma}^{P}$ respectively. An average parameter is represented by the bars or over-score. The existence of inclusion causes the strain field in the matrix to become non-uniform, as demonstrated in Fig. 2a. The average strain state in the matrix can be represented by the equation below.

$$\bar{\varepsilon}^{P} = \varepsilon_a + \bar{\varepsilon}^{Ppt} \tag{7}$$

As a result, the inclusion phase can go through a similar change, and the average state of strain in the inclusion can be represented by

$$\bar{\varepsilon}^{CNT} = \bar{\varepsilon}^{P} + \varepsilon^{CNTpt} \tag{8}$$

The abbreviation *pt* stands for perturbation. The relationship between the inhomogeneous inclusion in Fig. 2a and the homogeneous inclusion problem in Fig. 2b may be demonstrated by correlating the matrix and inclusion properties as follows, as stated by Eshelby [80]

$$\tilde{\sigma}^{CNT} = C^{CNT} : \bar{\varepsilon}^{CNT} = C^{P} : \left(\bar{\varepsilon}^{CNT} - \varepsilon^{*}\right) \tag{9}$$

where, ε^{*} denotes the inclusion's Eigen-strain, which is related to the inclusion perturbation strain by the equation

$$\varepsilon^{CNTpt} = S : \varepsilon^{*} \tag{10}$$

In Eq. (10) the Eshelby's tensor is denoted by S, and related words are included in Appendix A. The Eigen-strain in Eq. (9) may be readily derived as

$$\varepsilon^{*} = -S^{P} : \left(C^{CNT} - C^{P}\right) : \bar{\varepsilon}^{CNT} \tag{11}$$

In Eq. (11) the compliance tensor for polymer materials is S^{P}. By substituting Eq. (11) in Eq. (8) and using Eq. (10) the average state of strain of inclusion can be related to the average state of strain of matrix as

$$\bar{\varepsilon}^{CNT} = \left[I + S : S^{P} : \left(C^{CNT} - C^{P}\right)\right]^{-1} : \bar{\varepsilon}^{P} \tag{12}$$

The tensor that relates average strain in the inclusion to average strain in the matrix in Eq. (12) is known as the dilute strain concentration tensor and can be written as

$$A^{\text{dil}} = \left[I + S : S^{P} : \left(C^{CNT} - C^{P}\right)\right]^{-1} \tag{13}$$

I represents the fourth-order identity tensor in the previous Eqs. (12) and (13). Equation (12) may be written as

$$\bar{\varepsilon}^{CNT} = A^{\text{dil}} : \bar{\varepsilon}^{P} \tag{14}$$

The average strain ε_a contributes to the inclusion and matrix's average strain.

$$v_{NC}^{P}\bar{\varepsilon}^{P} + v_{NC}^{CNT}\bar{\varepsilon}^{CNT} = \varepsilon_a \tag{15}$$

In Eq. (15) the volume fractions of matrix and carbon nano tubes in the nano composite phase are v_{NC}^{P} and, v_{NC}^{CNT} respectively. By substituting Eq. (12) into Eq. (15), will give

$$\bar{\varepsilon}^{P} = \left[v_{NC}^{P} I + v_{NC}^{CNT} A^{\text{dil}}\right]^{-1} : \varepsilon_a \tag{16}$$

It is worth noting that the applied average strain and the matrix's average strain are now linked, and the Equation may express the strain concentration tensor. (17)

$$A_0 = \left[v_{NC}^{P} I + v_{NC}^{CNT} A^{\text{dil}}\right]^{-1} \tag{17}$$

As a result, Eq. (16) may be written as

$$\bar{\varepsilon}^{P} = A_0 : \varepsilon_a \tag{18}$$

After putting Eq. (18) in Eq. (14), the average strain tensor in the inclusion can be written in terms of applied average strains and average strains in the inclusion becomes

$$\bar{\varepsilon}^{CNT} = A^{\text{dil}} : A_0 : \varepsilon_a = A^{\text{ndil}} : \varepsilon_a \tag{19}$$

where, the non-dilute strain concentration tensor in Eq. (19) is denoted by, A^{ndil}. Similar to Eq. (15), in the case of an aligned inclusion, the average stress tensor of nanocomposite may be obtained as

$$v_{NC}^{P}\tilde{\sigma}^{P} + v_{NC}^{CNT}\tilde{\sigma}^{CNT} = \tilde{\sigma} = C^{NC} : \varepsilon_a \tag{20}$$

The effective stiffness tensor of the nanocomposite may be obtained by rearranging Eq. (20) with the information that, $\tilde{\sigma}^{P} = C^{P} : \bar{\varepsilon}^{P}$ and $\bar{\sigma}^{CNT} = C^{CNT} : \bar{\varepsilon}^{CNT}$.

$$C^{NC} = \left(v_{NC}^{P} C^{P} + v_{NC}^{CNT} C^{CNT} : A^{\text{dil}}\right) : \left(v_{NC}^{P} I + v_{NC}^{CNT} A^{\text{dil}}\right)^{-1} \tag{21}$$

The strain and stress of a CNTs or inclusion may be averaged in all conceivable directions for randomly oriented CNTs, and so Eq. (14) can be expressed as

$$\begin{aligned} \langle \bar{\varepsilon}^{CNT} \rangle &= \langle A^{\text{dil}} : \bar{\varepsilon}^{P} \rangle = \langle A^{\text{dil}} \rangle : \bar{\varepsilon}^{P} \\ \langle \tilde{\sigma}^{CNT} \rangle &= \langle C^{CNT} : A^{\text{dil}} \rangle : \bar{\varepsilon}^{P} \end{aligned} \tag{22}$$

Hence for randomly oriented CNTs, the Eq. (21) can be modified as

$$C^{NC} = \left(v_{NC}^{P} C^{P} + v_{NC}^{CNT} \langle C^{CNT} A^{\text{dil}} \rangle\right) : \left(v_{NC}^{P} I + v_{NC}^{CNT} \langle A^{\text{dil}} \rangle\right)^{-1} \tag{23}$$

The details about the bracket $\langle\rangle$ is given in Sect. 2.3.

2.3 Weak interface theory

To represent the WI, Qu [81] and Esteva and Spanos [76] used a linear spring layer with a negligible thickness, where traction was assumed to be continuous, and displacement was assumed to be discontinuous at the interfaces. The following equation may be used to represent both continuous traction and displacement jump.

$$\begin{aligned} \Delta\sigma_{ij} n_j &\equiv [\sigma_{ij}(S_l^{+}) - \sigma_{ij}(S_l^{-})] n_j = 0 \\ \Delta u_i &\equiv [u_i(S_l^{+}) - u_i(S_l^{-})] = \eta_{ij}\sigma_{jk} n_k \end{aligned} \tag{24}$$

The parameters S_l in the Eq. (24) indicate the interface and n is a unit vector that is normal and outward from it. $u_i(S_l^{+})$ and $u_i(S_l^{-})$ are the displacement amounts while approaching the inclusion from the inside and outside, respectively. The second-order (η_{ij}) accounts for the spring layer's compliance and is expressed as

$$\eta_{ij} = \alpha\delta_{ij} + (\beta - \alpha)n_i n_j \tag{25}$$

The cut section of CNTs inclusion in the polymer matrix is shown in Fig. 3, where both the normal and shear stresses are produced due to loading. Normal stress is generated in direction 1, whereas shear stress is induced in direction 3 at the thickness less interface. For the sake of simplicity in this problem, all stress components in the other direction are ignored. Hence all terms i.e., η_{ij} ($i, j = 2$) are ignored.

The indicial notations can be used to write expansions of the second part of the Eq. (24) for the nanocomposite section (shown in Fig. 3).

$$\begin{aligned} \Delta u_1 &= \eta_{11}\sigma_{11}n_1 + \eta_{11}\sigma_{13}n_3 + \eta_{13}\sigma_{31}n_1 + \eta_{13}\sigma_{33}n_3 \\ \Delta u_3 &= \eta_{31}\sigma_{11}n_1 + \eta_{31}\sigma_{13}n_3 + \eta_{33}\sigma_{31}n_1 + \eta_{33}\sigma_{33}n_3 \end{aligned} \tag{26}$$

In Eq. (26) $n_3 = 0$ and $n_1 = 1$. when the inclusion is oriented along direction '3' (as illustrated in Fig. 3). As a result, Eq. (26) is reduced to

$$\begin{aligned} \Delta u_1 &= \eta_{11}\sigma_{11}n_1 + \eta_{13}\sigma_{31}n_1 \\ \Delta u_3 &= \eta_{31}\sigma_{11}n_1 + \eta_{33}\sigma_{31}n_1 \end{aligned} \tag{27}$$

The terms, η_{11},η_{13},η_{31} and η_{33}. may be derived further from Eq. (25) as follows

$$\begin{aligned} \eta_{11} &= \alpha\delta_{11} + (\beta - \alpha)n_1 n_1 = \beta \\ \eta_{13} &= \alpha\delta_{13} + (\beta - \alpha)n_1 n_3 = 0 \\ \eta_{31} &= \alpha\delta_{31} + (\beta - \alpha)n_3 n_1 = 0 \\ \eta_{33} &= \alpha\delta_{33} + (\beta - \alpha)n_3 n_3 = \alpha \end{aligned} \tag{28}$$

Putting Eq. (28) in Eq. (27), which produces

$$\begin{aligned} \Delta u_1 &= \beta\sigma \\ \Delta u_3 &= \alpha\tau \end{aligned} \tag{29}$$

The Eq. (29) may be used to calculate the tangential and normal compliances (such as α and β). The Eshelby's tensor may be calculated using WI theory [76, 81] as

$$\overline{S}_{ijkl} = S_{ijkl} + \left(I_{ijpq} - S_{ijpq}\right)H_{pqrs}C^{P}_{rsmn}\left(I_{mnkl} - S_{mnkl}\right) \tag{30}$$

where H is given by

$$H_{ijkl} = \alpha P_{ijkl} + (\beta - \alpha)Q_{ijkl} \tag{31}$$

Appendix B contains a list of other unknown terms in the Eq. (31). As a result, Eq. (21) is rewritten to become

$$\begin{aligned} C^{NC} = &\left(v^{P}_{NC}C^{P} + v^{CNT}_{NC}C^{CNT} : \overline{A}^{\text{dil}}\right) : \\ &\left[v^{P}_{NC}I + v^{CNT}_{NC}\left(\overline{A}^{\text{dil}} + H : C^{CNT} : \overline{A}^{\text{dil}}\right)\right]^{-1} \end{aligned} \tag{32}$$

were,

$$\overline{A}^{\text{dil}} = \left[I + \overline{S} : S^{P} : \left(C^{CNT} - C^{P}\right)\right]^{-1} \tag{33}$$

At this point Eq. (32) gives the property of nanocomposite or modified matrix which is transversely isotropic in nature depending on the orientation of inclusion. For modified matrix or the nanocomposite phase where the inclusions with weak interphase are randomly oriented, the effective property can be obtained by averaging the property as done in Eq. (23). So the Eq. (32) for randomly oriented inclusion may be written as

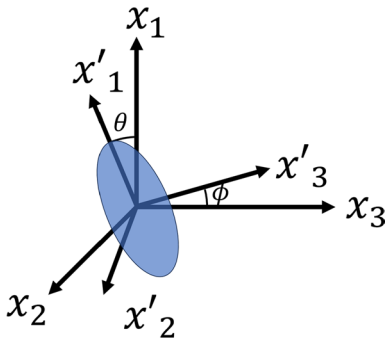

Fig. 4 Inclusion in local and global coordinate system

$$C^{NC} = \left(v_{NC}^{P} C^{P} + v_{NC}^{CNT} \langle C^{CNT} : \overline{A}^{\text{dil}} \rangle\right) : \left(v_{NC}^{P} I + v_{NC}^{CNT} \langle \overline{A}^{\text{dil}} \rangle + v_{NC}^{CNT} \langle H : C^{CNT} : \overline{A}^{\text{dil}} \rangle\right)^{-1} \tag{34}$$

Both in Eqs. (23) and (34) the terms within this bracket $\langle\rangle$ indicate that it has been averaged over the volume. To predict the behaviour of a system characterized by a three-dimensional random fiber orientation, it is necessary to establish a correspondence between the local coordinates of particles and the global coordinates of composites, as seen in Fig. 4. The primed coordinate system represents the local axis of a spheroid inclusion, whereas the unprimed coordinate system represents the global. If the axis of the inclusion is along the $x_1\prime$. The co-ordinate transformation from the local $\boldsymbol{x'}$ to global $\boldsymbol{x}$ can be represented by $\{x_i\prime\} = [Q_{ij}]\{x_j\}$. Where $[Q]$ is given as follows [82].

$$\begin{bmatrix} cos\theta & sin\theta cos\phi & sin\theta sin\phi \\ -sin\theta & cos\theta cos\phi & cos\theta sin\phi \\ 0 & -sin\phi & cos\phi \end{bmatrix} \tag{35}$$

As per Fig. 4, the θ can vary from 0 to $\pi/2$ where ϕ can be varied from 0 to 2π for any possible orientation in the global coordinate. Therefore, the determination of any material constants $\langle L_{ijkl} \rangle$ for a composite with 3D randomly oriented inclusions may be achieved using equation Eq. (36).

$$\langle L_{ijkl} \rangle = \frac{1}{2\pi} \int_0^{2\pi} \int_0^{\frac{\pi}{2}} Q_{mi} Q_{nj} L_{mnpq} Q_{pk} Q_{ql} \sin\theta d\theta d\phi \tag{36}$$

2.4 Agglomeration effects of CNTs

When the fraction of CNTs in the polymer phase gets large, there is always the possibility of CNTs clubbing to form clusters in the polymer. This is referred to as CNTs aggregation/ agglomeration. Figure 5 shows the formed cluster in the nanocomposite phase.

$$V_{NC}^{CNT} = V_{cluster}^{CNT} + V_{P}^{CNT} \tag{37}$$

The cluster is a spherical inclusion with randomly arranged transversely isotropic CNTs, resulting cluster's property being isotropic. The resultant phase must be isotropic since the isotropic clusters are present in an isotropic phase (specifically *NC*). If V_{NC}^{CNT} represent the total volume of total CNTs, and it may be separated into two components [75]. Where, $V_{Cluster}^{CNT}$ represents the volume of CNTs trapped inside the cluster, and, V_{P}^{CNT} represents the remaining CNTs in the polymer phase outside of the cluster. The following are the agglomeration constants [75] defined as

$$\xi = \frac{V^{cluster}}{V^{NC}}; \quad \zeta = \frac{V_{\text{cluster}}^{\text{CNT}}}{V_{\text{NC}}^{\text{CNT}}} \tag{38}$$

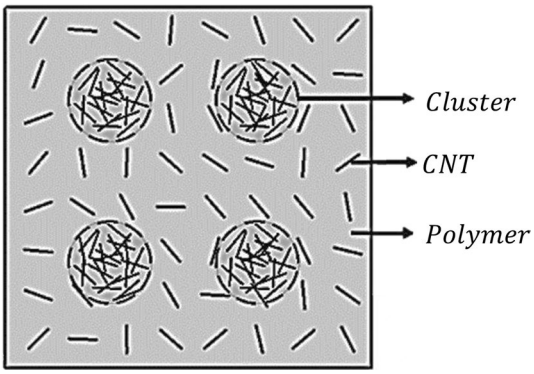

Fig. 5 RVE showing CNT, clusters and polymer phases

As a result, ξ denotes the volume fraction of the spherical cluster relative to the RVE, and ζ represents the volume of CNTs trapped in the spherical cluster as a percentage of total CNTs in the RVE. As per Eq. (38), CNTs are said to be uniformly dispersed in the matrix when $\xi = 1$CNTs are uniformly dispersed in the matrix and the equation also implies that lower the value of ξ, the more severe will be the degree of CNTs aggregation. When $\zeta = 1$, all the CNTs are considered to be concentrated in the inclusion, but as ζ decreases, the concentration of CNTs in the cluster declines. CNTs, on the other hand, are are evenly dispersed throughout the matrix when $\xi = \zeta$. From Eqs. (37) and (38) can be solved for the volume fraction of CNTs trapped inside the cluster with respect to the spherical cluster and can be represented as

$$v_{cluster}^{CNT} = \frac{\zeta}{\xi} v_{NC}^{CNT} \tag{39}$$

As a result, the elastic property of the spherical cluster may be determined using the equation below.

$$\begin{aligned} C^{NC}\big|_{in} = &\left((1 - v_{cluster}^{CNT})C^{P} + v_{cluster}^{CNT}\langle C^{CNT} : \overline{A}^{\text{dil}}\rangle\right) : \\ &\left((1 - v_{cluster}^{CNT})I + v_{cluster}^{CNT}\langle \overline{A}^{\text{dil}}\rangle + v_{cluster}^{CNT}\langle H : C^{CNT} : \overline{A}^{\text{dil}}\rangle\right)^{-1} \end{aligned} \tag{40}$$

The volume fraction of CNTs in the polymer phase but outside the cluster may be calculated to be

$$v_{P}^{CNT} = \left(\frac{1 - \zeta}{1 - \xi}\right) v_{NC}^{CNT} \tag{41}$$

Based on Eq. (41), the elastic property outside of the spherical cluster may be computed as

$$\begin{aligned} C^{NC}\big|_{out} = &\left((1 - v_{p}^{CNT})C^{P} + v_{p}^{CNT}\langle C^{CNT} : \overline{A}^{\text{dil}}\rangle\right) : \\ &\left((1 - v_{p}^{CNT})I + v_{p}^{CNT}\langle \overline{A}^{\text{dil}}\rangle + v_{p}^{CNT}\langle H : C^{CNT} : \overline{A}^{\text{dil}}\rangle\right)^{-1} \end{aligned} \tag{42}$$

Finally, the effective elastic property of the *NC* phase may be determined, which takes into account the weak interphase and agglomeration as [66, 83, 84]

$$\begin{aligned} C^{NC} = &\left((1 - \xi)C^{NC}\big|_{out} + \xi\langle C^{NC}\big|_{in} : \overline{\overline{A}}^{\text{dil}}\rangle\right) : \\ &\left((1 - \xi)I + \xi\langle \overline{\overline{A}}^{\text{dil}}\rangle + \xi\langle H : C^{NC}\big|_{in} : \overline{\overline{A}}^{\text{dil}}\rangle\right)^{-1} \end{aligned} \tag{43}$$

and

$$\overline{\overline{A}}^{\text{dil}} = \left[I + \overline{S} : S^{NC}\Big|_{out} : \left(C^{NC}\Big|_{in} - C^{NC}\Big|_{out}\right)\right]^{-1} \tag{44}$$

2.5 Correspondence principle for the weak interface

The compliances (η_{ij}) in Eq. (25) for a viscoelastic material are time-dependent, and this can be achieved by representing α and β as a function of time. As a result, Eq. (25) may be written as

$$\eta_{ij}(t) = \alpha(t)\delta_{ij} + (\beta(t) - \alpha(t))n_i n_j \tag{45}$$

As a result, the displacement jump becomes time-dependent and can be represented as

$$\Delta u_i(t) = \int_{-\infty}^{t} \eta_{ij}(t-\Gamma)\frac{\partial \sigma_{jk}(\Gamma)}{\partial \Gamma} d\Gamma . \Delta n_k \tag{46}$$

Invoking Eq. (2), the correspondence principle may be used to transform Eq. (46) to the frequency domain, and it can be expressed as

$$\Delta u_i(\omega) = \int_0^{\infty} \left[\int_{-\infty}^{t} \eta_{ij}(t-\Gamma)\frac{\partial \sigma_{jk}(\Gamma)}{\partial \Gamma} d\Gamma \right] e^{-i\omega t} dt . \Delta n_k \tag{47}$$

Which results

$$\begin{aligned} \Delta u_1(\omega) &= \int_0^{\infty} \left[\int_{-\infty}^{t} \beta(t-\Gamma)\frac{\partial \sigma(\Gamma)}{\partial \Gamma} d\Gamma \right] e^{-i\omega t} dt \cdot \Delta n_3 \\ \Delta u_3(\omega) &= \int_0^{\infty} \left[\int_{-\infty}^{t} \alpha(t-\Gamma)\frac{\partial \tau(\Gamma)}{\partial \Gamma} d\Gamma \right] e^{-i\omega t} dt \cdot \Delta n_1 \end{aligned} \tag{48}$$

The viscoelastic compliance of and is frequency dependent α and β may be expressed as

$$\begin{aligned} \alpha(\omega) &= \alpha'(\omega) - i\alpha''(\omega) \\ \beta(\omega) &= \beta\prime(\omega) - i\beta''(\omega) \end{aligned} \tag{49}$$

For CNTs, β can be assumed to be zero [66, 76, 83–85], and the compliance α can be represented in terms of a dimensionless parameter α_0, diameter of CNTs and viscoelastic shear modulus $G(\omega)$ of polymer phase as follows

$$\alpha(\omega) = \frac{\alpha_0 d_{cnt}}{|G(\omega)|}\left\{ 1 - i\frac{\alpha''}{\alpha'} \right\} \tag{50}$$

Here, d_{cnt} is the diameter of CNTs and α_0 implies the magnitude of $\alpha\prime$ whereas the ratio $\alpha^{''}/\alpha\prime$ represents interfacial loss factor.

2.6 Elastic properties of individual yarn

SOM may be used to determine the effective viscoelastic properties of *NCF* phase which is formed by combining *NC* phase and along with *F*. As shown in Fig. 1, the axis of transverse isotropy along axis '1' while considering *NCF* phase. Considering the iso-field condition and the rules of mixture, the state of stresses and strains for the individual constituents' *NC* and *F* phases are related to the state of stress and strain of *NCF* phase.

$$\begin{gathered}\varepsilon_1^{NCF}=\varepsilon_1^{NC}=\varepsilon_1^{F}\\ \left\{\begin{array}{c}\sigma_2^{NCF}\\ \sigma_3^{NCF}\\ \sigma_{23}^{NCF}\\ \sigma_{13}^{NCF}\\ \sigma_{12}^{NCF}\end{array}\right\}=\left\{\begin{array}{c}\sigma_2^{NC}\\ \sigma_3^{NC}\\ \sigma_{23}^{NCF}\\ \sigma_{13}^{NC}\\ \sigma_{12}^{NC}\end{array}\right\}=\left\{\begin{array}{c}\sigma_2^{F}\\ \sigma_3^{F}\\ \sigma_{23}^{F}\\ \sigma_{13}^{F}\\ \sigma_{12}^{F}\end{array}\right\}\\ \sigma_1^{NCF}=v_{NCF}^{NC}\sigma_1^{NC}+v_{NCF}^{F}\sigma_1^{F}\\ \left\{\begin{array}{c}\varepsilon_2^{NCF}\\ \varepsilon_3^{NCF}\\ \varepsilon_{23}^{NCF}\\ \varepsilon_{13}^{NCF}\\ \varepsilon_{12}^{NCF}\end{array}\right\}=v_{NCF}^{NC}\left\{\begin{array}{c}\varepsilon_2^{NC}\\ \varepsilon_3^{NC}\\ \varepsilon_{23}^{NC}\\ \varepsilon_{13}^{NC}\\ \varepsilon_{12}^{NC}\end{array}\right\}+v_{NCF}^{F}\left\{\begin{array}{c}\varepsilon_2^{F}\\ \varepsilon_3^{F}\\ \varepsilon_{23}^{F}\\ \varepsilon_{13}^{F}\\ \varepsilon_{12}^{F}\end{array}\right\}\end{gathered} \tag{51}$$

where v_{NCF}^{NC} and v_{NCF}^{F} are the volume fraction of *NC* and carbon fibre (*F*) with respect to *NCF* which is related by $v_{NCF}^{NC}+v_{NCF}^{F}=1$.The constitutive relation of individual constituents in *NCF* can be written as

$$\left\{\sigma^k\right\}=\left[C^k\right]\left\{\varepsilon^k\right\};\quad k=NC,F\ and\ NCF \tag{52}$$

The Eqs. (51) and (52) together give the constitutive relation for *PMNCF* as follows

$$\left[C^{NCF}\right]=\left[C_1\right]\left[V_1\right]^{-1}+\left[C_2\right]\left[V_2\right]^{-1} \tag{53}$$

The individual terms used in Eq. (53) such as $\left[C_1\right],\left[V_1\right],\left[C_2\right]$ and $\left[V_2\right]$ are defined in the Appendix C.

2.7 Elastic properties of the representative unit cell (*RUC*)

Figure 6 shows the detailed constructional feature of the *RUC*. As can be seen from Fig. 6

the fill yarn, warp yarn, and the polymer are the *RUC*'s primary constituents. The yarns are lenticular in cross-section with the radius of curvature, thickness, and breadth given by r_k, t_k and $S_{Fk}t_k$ respectively, as shown in section 'a-b-c-d-a'. It may be deduced from section 'e-f-g-h-e' that the yarn-to-yarn distance is l_k and the gap between two yarns is l_{gk} and $\left(l_{gk}\right)_{\min}$ is the smallest possible gap between two yarns. The crimp angle of the yarn is represented by β_{ck} where, subscript *k* represents

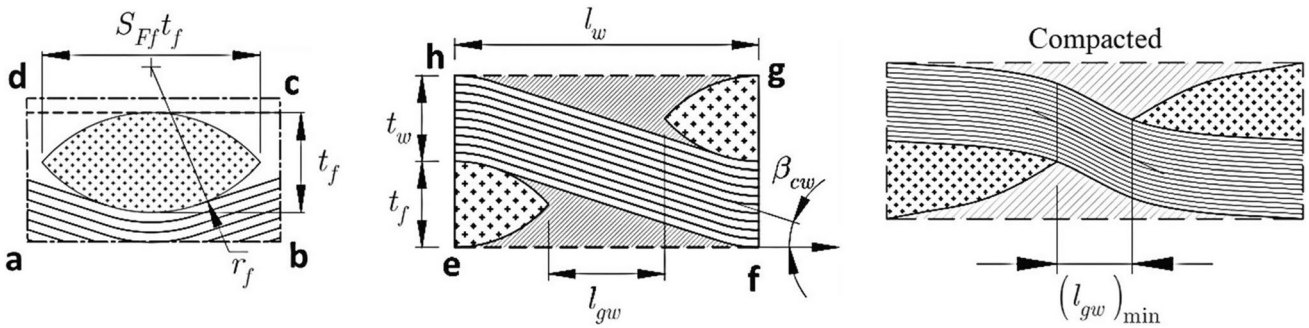

Fig. 6 Sectional view of *RUC*

either the warp or fill ($k = w, f$). The radius, inner angle, and area of a lenticular wrap yarn may be represented based on the geometry of lenticular sectional view as

$$\begin{aligned} r_w &= \frac{t_w\left(1+S_{Fw}^2\right)}{4} \\ \alpha_w &= 2\arcsin\left(\frac{2S_{Fw}}{1+S_{Fw}^2}\right) \\ A_w &= r_w^2\left(\alpha_w - \sin\alpha_w\right) \end{aligned} \tag{54}$$

The yarn to yarn distance is clearly shown in Fig. 6 as

$$L_w = S_{Ff}t_f + L_{gw} \tag{55}$$

It is also worth noting that, as shown in Fig. 6, the specified gap length for a tightly packed/ compressed composite laminate cannot be zero. For a tightly packed/ compressed composite laminate, the shortest gap length is

$$\left(L_{gw}\right)_{\min} = \left(2r_f + t_w\right)\sin\beta_w - S_{Ff}t_f \tag{56}$$

$$\text{where, } \beta_w\big|_{\left(L_{gw}\right)_{\min}} = \arccos\left(\frac{2r_f + t_w - t_f}{2r_f + t_w}\right) \tag{57}$$

The yarn crimp angle for wrap yarn (β_{cw}) may be calculated as

$$\begin{aligned} \beta_{cw} &= \arcsin\left(\frac{2r_f + t_w}{\sqrt{L_w^2 + \left(2r_f + t_w - t_f\right)^2}}\right) - \beta_{ow} \\ \textit{where, } \beta_{ow} &= \arctan\left(\frac{2r_f + t_w - t_f}{L_w}\right) \end{aligned} \tag{58}$$

The length partition of the crimp part with respect to the total length of wrap yarn can be expressed as

$$\mu_{cw} = \frac{\left(2r_f + t_w\right)\sin\left(\beta_{cw}\right)}{L_w} \tag{59}$$

where the straight portion length of the wrap yarn is expressed as

$$L_{sw} = \sqrt{L_w^2 + t_f^2 - 2t_f\left(2r_f + t_w\right)} \tag{60}$$

As a result, the volume of the wrap yarn is calculated using the lengths of the curved, the straight portions, and the area of the wrap yarn, which may be expressed as

$$V_{yw} = 4A_w\left\{\left(2r_f + t_w\right)\beta_{cw} + L_{sw}\right\} \tag{61}$$

Similarly, by changing the subscript from '*w*' to '*f*' in Eqs. (54)–(61), one can get different fill yarn parameters. Given the volume of the RUC $V_{RUC} = 4\left(t_w + t_f\right)L_wL_f$ the actual volume fraction of *NCF* with respect to the RUC can be calculated using the following expression.

$$v_{RUC}^{NCF} = pf \times \frac{V_{yf} + V_{yw}}{V_{RUC}} \tag{62}$$

where, *pf* denotes the fibre's packing fraction. It is self-evident that $v_{RUC}^{NCF} + v_{RUC}^{NC} = 1$, and it is also evident that hexagonal packing is used to calculate packing fraction. v_{RUC}^{NCF} from Eq. (62) and iso-field condition in conduction with rules of mixture the compliance, $S\prime_w$ can be evaluated considering the axis of transverse isotropy along the axis of the wrap yarn.

After appropriate transformation and orientation averaging can be applied on $S\prime_w$ to get the averaged compliance $S_{\overline{w}}$ as follows.

$$S_{\overline{w}} = \frac{1}{\beta}\int_0^{\beta_{cw}} T_{r2}^t S\prime_w T_{r2}^t d\beta \tag{63}$$

The transformation matrices, T_{r2} has been considered to transform $S\prime_w$ about the axis '2'. In the Eq. (63), the individual terms of transformed compliance $S_{\overline{w}}$ are as follows:

$$\begin{aligned}
&S_{\bar{w}}(1,1) = \frac{\left\{A_{\bar{w}}S'_{11} + B_{\bar{w}}S'_{33} + C_{\bar{w}}\left(S'_{13}+S'_{31}+S'_{55}\right)\right\}}{\beta_{cw}}; S_{\bar{w}}(1,2) = \frac{\left(D_{\bar{w}}S'_{12} + E_{\bar{w}}S'_{32}\right)}{\beta_{cw}};\\
&S_{\bar{w}}(1,3) = \frac{\left\{A_{\bar{w}}S'_{13} + B_{\bar{w}}S'_{31} + C_{\bar{w}}\left(S'_{11}+S'_{33}-S'_{55}\right)\right\}}{\beta_{cw}}; S_{\bar{w}}(2,3) = \frac{\left(E_{\bar{w}}S'_{21} + D_{\bar{w}}S'_{23}\right)}{\beta_{cw}};\\
&S_{\bar{w}}(1,5) = \frac{\left\{F_{\bar{w}}\left(S'_{13}-S'_{11}\right) + G_{\bar{w}}\left(S'_{31}-S'_{33}\right) + H_{\bar{w}}S'_{55}\right\}}{\beta_{cw}}; S_{\bar{w}}(2,5) = \frac{2I_{\bar{w}}\left(S'_{21}-S'_{23}\right)}{\beta_{cw}};\\
&S_{\bar{w}}(2,2) = S\prime_{22}; S_{\bar{w}}(3,3) = \frac{\left\{B_{\bar{w}}S'_{11} + A_{\bar{w}}S'_{33} + C_{\bar{w}}\left(S'_{13}+S'_{31}+S'_{55}\right)\right\}}{\beta_{cw}};\\
&S_{\bar{w}}(3,5) = \frac{\left\{F_{\bar{w}}\left(S'_{33}-S'_{31}\right) + G_{\bar{w}}\left(S'_{11}-S'_{13}\right) + H_{\bar{w}}S\prime_{55}\right\}}{\beta_{cw}};\\
&S_{\bar{w}}(4,4) = \frac{\left(D_{\bar{w}}S'_{44} + E_{\bar{w}}S'_{66}\right)}{\beta_{cw}}; S_{\bar{w}}(4,6) = \frac{I_{\bar{w}}\left(S'_{66}-S'_{44}\right)}{\beta_{cw}};\\
&S_{\bar{w}}(5,5) = \frac{\left\{J_{\bar{w}}\left(S'_{11}-S'_{13}-S'_{31}+S'_{33}\right) + K_{\bar{w}}S'_{55}\right\}}{\beta_{cw}};\\
&S_{\bar{w}}(6,6) = S'_{\bar{w}}(4,4)
\end{aligned} \tag{64}$$

Appendix D contains a list of the associated terms in Eq. (64). Individual terms of $S_{\overline{f}}$ are also computed in the same way by transforming and averaging $S\prime_f$ about axis '1'. The wrap yarn's effective elastic compliance matrix S_W may be determined by

$$S_W = \mu_{cw}S_{\overline{w}} + \left(1-\mu_{cw}\right)S\prime_{\overline{w}} \tag{65}$$

Volume averaging may be used to evaluate the RUC's effective in-plane stiffness (C^I_{RUC}) and out of plane compliance (S^O_{RUC}).

$$\begin{aligned}
S^O_{RUC} &= S_W\left(\frac{V_{yw}}{V_{yf}+V_{yw}}\right) + S_F\left(\frac{V_{yf}}{V_{yf}+V_{yw}}\right)\\
C^I_{RUC} &= C_W\left(\frac{V_{yw}}{V_{yf}+V_{yw}}\right) + C_F\left(\frac{V_{yf}}{V_{yf}+V_{yw}}\right)
\end{aligned} \tag{66}$$

where C_k is the inverse of S_k by taking $k = W$ and F. Finally, the effective elastic properties from Eq. (66) are obtained as follows.

$$\begin{aligned}
&E_1 = \frac{1}{S^I_{RUC}(1,1)}; \quad E_2 = \frac{1}{S^I_{RUC}(2,2)}; \quad E_3 = \frac{1}{S^O_{RUC}(3,3)};\\
&G_{12} = \frac{1}{S^I_{RUC}(6,6)}; \quad G_{23} = \frac{2}{\left\{S^O_{RUC}(4,4) + S^I_{RUC}(4,4)\right\}}; \quad G_{31} = \frac{2}{\left\{S^O_{RUC}(5,5) + S^I_{RUC}(5,5)\right\}}\\
&\nu_{12} = \frac{-S^O_{RUC}(1,2)}{S^I_{RUC}(1,1)}; \quad \nu_{23} = \frac{-S^O_{RUC}(3,2)}{S^I_{RUC}(3,3)};
\end{aligned} \tag{67}$$

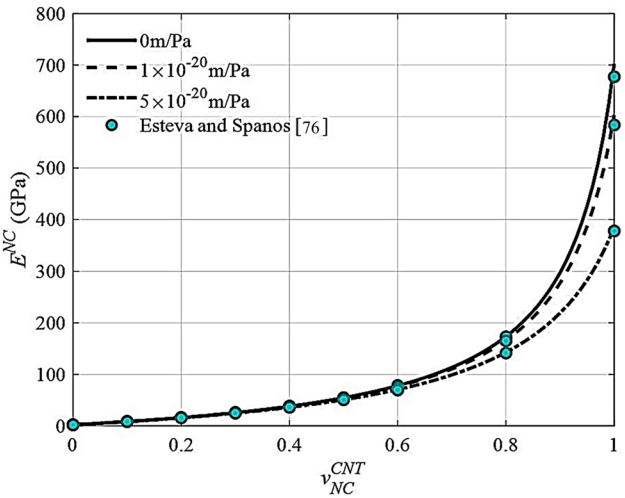

Fig. 7 Young's modulus variation with carbon nanotubes for different interfacial compliance

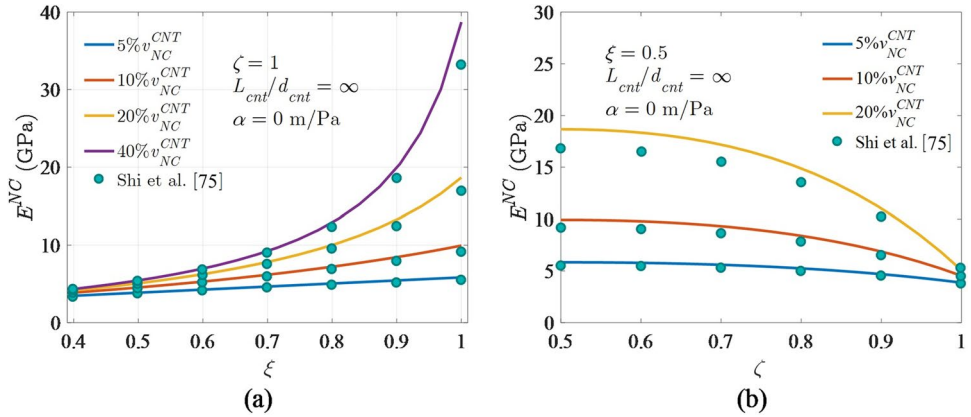

Fig. 8 Young's modulus variation with agglomeration parameters **a** ζ and **b** ξ for different CNT content

3 Results and discussions

A MATLAB programme has been developed for material modelling based on mathematical formulas discussed in the previous sections. Based on the formulations, the composite material system, as represented in Fig. 1, has three basic sub-material systems such as 1. *NC* phase (modified matrix) formed by adding *CNT* and polymer, 2. Yarn formed by *NC* phase and fibre, and finally, 3. Combination of undulated yarn and polymer phase (*RUC*). The proposed micromechanical framework needs validation at the sub-component level; hence, three validation stages were adopted, where the first two validation stages were conducted for the *NC* phase with and without agglomeration. The second phase of validation was carried out for yarns and *RUC*. After the validation, the novel micromechanics was utilised for further studies.

3.1 Material property validation

The elastic properties of nanocomposite for various interfacial compliance values were investigated using Eq. (43), as illustrated in Fig. 7. The material parameters of the nanocomposite constituents used in this validation stage were obtained from Ref. [76, 79]. The Young's modulus of nanocomposites found is quite similar to Esteva and Spanos' findings [76], as shown in Fig. 7 where l_{cnt}/d_{cnt} is equal to 50 and d_{cnt} is considered as 1.7 nm.

Another validation is carried out to assess the correctness of the suggested formulation based on published nanocomposite [75] results when agglomeration is considered. The CNTs are assumed to be entirely bound to the matrix in this case (i.e.. $\alpha = 0$). This validation's attributes are also obtained from Ref. [75], with the l_{cnt}/d_{cnt} value being ∞. Figure 8a, b demonstrate that the proposed formulation can produce outstanding results similar to those reported by Shi et al. [75].The proposed formulation, as shown in Fig. 8a, b, can produce outstanding results that

are similar to those achieved by Shi et al. [75]. The negligible variance may be due to matrix manipulation rather than the explicit expression offered by Shi et al. [75].

3.2 Validation of elastic characteristics

Plane woven composite material, which consists of carbon fibre as reinforcement and aluminium metal as the matrix, was used to validate the formulations, and the results are shown in Table 1. Table 1 illustrates that the findings are in accordance with prior study published in Ref. [86].

Table 1 Comparison of Geometric parameters and mechanical properties

Work →	Lee et al. [86]		Present
Parameter ↓	Theoretical	Experimental	
E_1 (GPa)	98.9	95.0	94.3042
E_2 (GPa)	92.8	90.7	88.0000
E_3 (GPa)	62.1	58.0	56.1766
G_{12} (GPa)	25.2	22.6	25.2349
G_{23} (GPa)	23.0	20.7	22.3611
G_{31} (GPa)	24.4	19.5	22.8255
v_{12}	0.24	0.21	0.2307
v_{23}	0.43	0.40	0.4054
v_{31}	0.20	0.20	0.2148
β_{cw} (Degree)	7.00	7.54	7.0037
β_{cf} (Degree)	7.46	7.78	7.4650
L_w (mm)	2.35	2.73	2.3407
L_f (mm)	2.63	2.72	2.6213
v_{RUC} (% age)	35.1	37.0	35.16

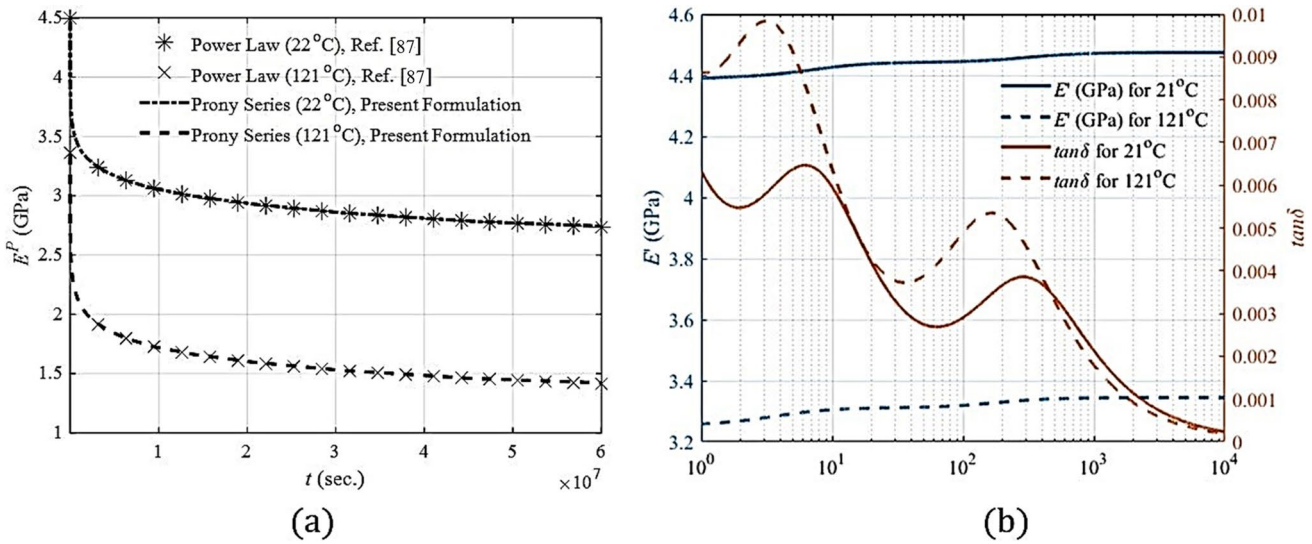

Fig. 9 **a** Power Law and the Prony series fit of the relaxation modulus **b** Storage modulus and loss factor for 934 Epoxy

3.3 Viscoelastic properties of individual constituents of material system

934 Epoxy has been chosen as the matrix material for which the creep compliance was modelled with a power-law model as $M^P(t) = D_0 + D_1 t^n$ and individual parameters of the model for different temperatures have been taken from Ref. [87]. The stress relaxation modulus ($E^P(t)$) has been numerically estimated with sufficient accuracy using eleven Prony series parameters, as illustrated in Fig. 9a. The parameters for the Prony series are also listed in Table 2. By utilising these parameters of the Prony series, storage modulus and loss factor for 934 Epoxy were evaluated, which are shown in Fig. 9b. Figure 9a demonstrates a decline in the relaxation modulus of the polymer as time and temperature rise, whereas Fig. 9b indicates an increase in the storage modulus with higher frequencies. Conversely, when the temperature rises, there is a corresponding drop. Consequently, the polymer exhibits a glassy behavior at higher frequencies and lower temperatures, whereas it displays a lathery behavior at lower frequencies and higher temperatures. The influence of time and frequency on the viscoelastic characteristics of the polymer is evident in Fig. 9a, b, whereas the thermoelastic properties of the polymer exhibit a gradual and more mild effect. Other constituent material properties (such as SWCNTs (10,10) and carbon fibre) are used from the available literature [86, 88–92] and treated as perfectly elastic in the current studies.

3.4 Problem specifications

The effects of several parameters on viscoelastic storage moduli and loss factors have been explored by varying CNTs volume fractions (v_{NC}^{CNT}), non-dimensional CNTs-polymer interphase compliance (α_0), CNTs- polymer interphase loss factor (α''/α'), agglomeration parameters (ζ and ξ), the aspect ratio of CNTs (l_{cnt}/d_{cnt}), and temperature (T in $^{\circ}$C) and excitation frequency (ω), the thickness of yarn (t_f), the width of yarn ($S_{Ff}t_f$), the ratio of gap length to width of

Table 2 Coefficients of Prony series for 934 Epoxy [87]

Temperature	22 °C		121 °C	
i	E_i^P	τ_i^P	E_i^P	τ_i^P
∞	2,662,987,567.34533		1,349,975,132.53024	
1	31,946,874.76110	0.00318	33,099,418.36941	0.00555
2	49,018,280.61009	0.14131	54,921,781.93832	0.27136
3	71,104,573.33824	3.45918	84,128,339.35263	6.45715
4	98,525,506.12263	57.28423	120,697,032.39106	99.30141
5	131,244,467.15976	718.90630	163,298,090.01449	1135.21594
6	168,295,436.39346	7329.32500	208,326,889.33604	10,457.53608
7	207,787,173.05179	63,467.54972	250,443,122.02547	81,746.19867
8	247,382,936.60221	482,907.43713	283,717,854.54735	563,853.53571
9	294,344,495.42045	3,385,519.05366	314,527,790.33682	3,616,027.08768
10	511,764,382.06722	31,518,411.26350	481,410,103.45771	30,734,238.59700

Table 3 Variation of parameters

Subsections	v_{NC}^{CNT} (%)	pf (%)	$\frac{l_{cnt}}{d_{cnt}}$	α_0	$\frac{\alpha''}{\alpha'}$	ζ	ξ	T ($^{\circ}$C)	ω (rad/sec)	$S_{Ff}t_f = S_{Fw}t_w\ t_f = t_w$ (mm) (mm)		$\frac{L_{gw}}{S_{Ff}t_f} = \frac{L_{gf}}{S_{Fw}t_w}$
3.4.1	V	V	50	1.2	0.2	0.7	0.5	22	10	6	0.6	0.4
3.4.2	V	60	V	1.2	0.2	0.7	0.5	22	10	6	0.6	0.4
3.4.3	V	60	50	V	0.2	0.7	0.5	22	10	6	0.6	0.4
3.4.4	V	60	50	1.2	V	0.7	0.5	22	10	6	0.6	0.4
3.4.5	V	60	50	1.2	0.2	V	0.5	22	10	6	0.6	0.4
3.4.6	V	60	50	1.2	0.2	0.7	V	22	10	6	0.6	0.4
3.4.7	20	60	50	1.2	0.2	0.7	0.5	V	V	6	0.6	0.4
3.4.8	20	60	50	1.2	0.2	0.7	0.5	22	10	V	V	0.4

V suggest variation in the parameter

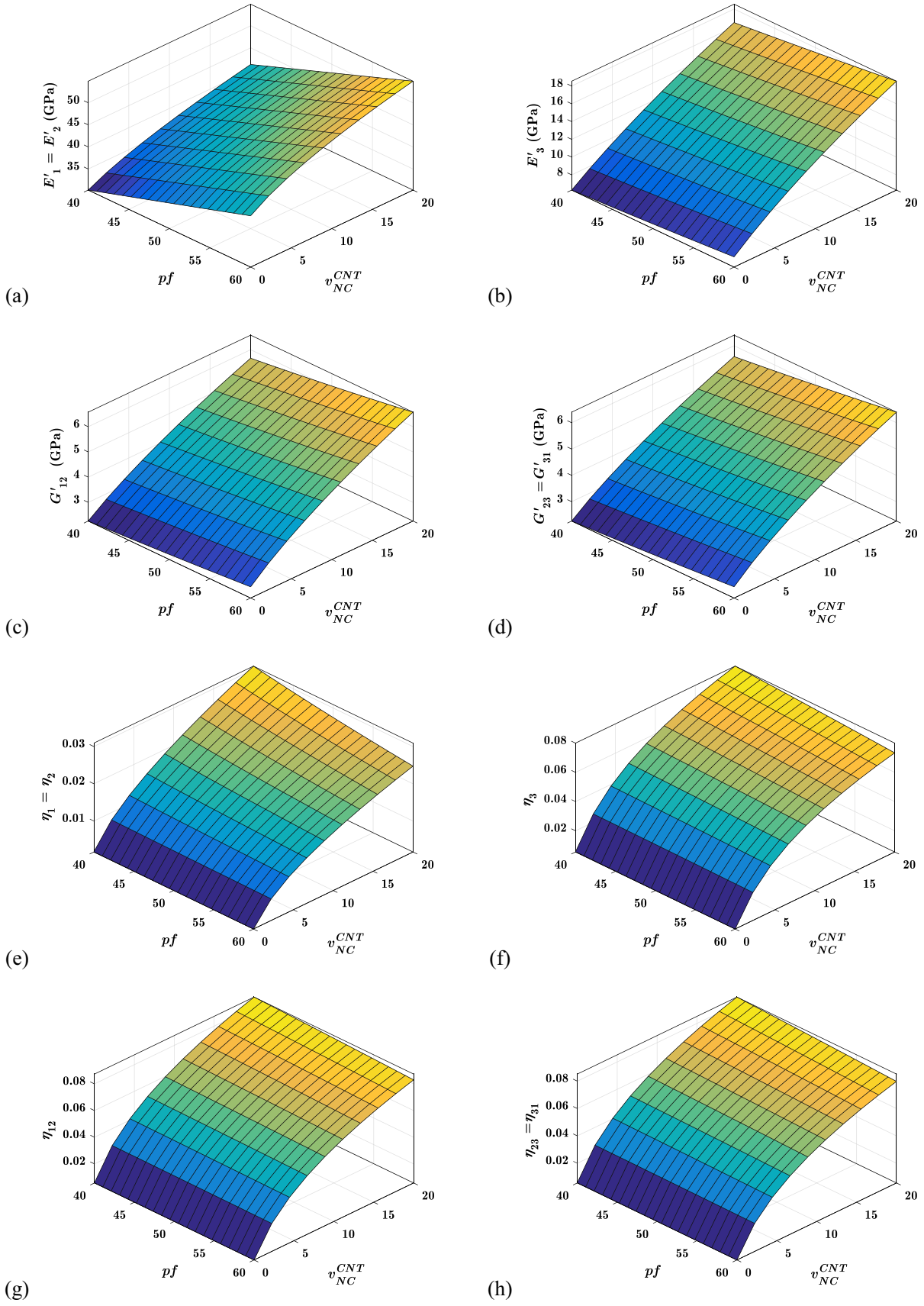

Fig. 10 Variation of the viscoelastic properties with v_{NC}^{CNT} and *pf*

yarn ($L_{gw}/S_{Ff}t_f$) and the fibre packing factor (pf). The range of the variation of parameters is listed in Table 3.ffects of carbon nanotube content ($\boldsymbol{v_{NC}^{CNT}}$) and fibre content ($\boldsymbol{pf}$) on the viscoelastic properties.

3.4.1 Effects of CNT conten (v_{NC}^{CNT}) and packing factor (pf) on the viscoelastic properties

The viscoelastic property of suggested hybrid nanocomposite materials for different fibre packing factors and CNTs concentrations are shown in Fig. 10. The in-plane and out-of-plane storage moduli improve with the fibre packing factor and CNTs content, as shown in Fig. 10a–d. The increase in the content of CNTs and fibres in the RUC is responsible for improving storage moduli. The in-plane storage moduli $E_1\prime$ and $E_2\prime$ are significantly more impacted by the CNTs content v_{NC}^{CNT} and packing factor pf, than other storage moduli, as shown in Fig. 10a–d. In contrast, the in-plane and out-of-plane loss factors improve with a rise in CNTs content v_{NC}^{CNT}. But worsen with an increase in fibre packing factor pf, as shown in Fig. 10e–h. This is because of an increase in the pf causes the NC phase to be squeezed out of the warp and fill yarn. The NC phase improves the RUC's damping performance. As the volume of the NC phase in both yarns decreases, the loss factors have deteriorated with the increase in pf.

3.4.2 Effects of aspect ratio (l_{cnt}/d_{cnt}) of CNTs on the viscoelastic properties

For various aspect ratios of CNTs (l_{cnt}/d_{cnt}) and CNTs concentrations, Fig. 11 shows the viscoelastic properties of the proposed hybrid nanocomposite material system. The addition of high aspect ratio CNTs improves all in-plane and out-of-plane storage moduli, as shown in Fig. 11a–d.

The rationale for this phenomenon is that longer CNTs can have stronger CNTs-polymer contact, resulting in higher stress transfer between the two separate phases due to their high aspect ratio. However, as shown in Fig. 11e–h, the in-plane and out-of-plane loss factors do not necessarily rise as the aspect ratio increases. For lower-value CNTs contents, the loss factor increases with increasing aspect ratio and remains constant. When the CNTs content is raised, the suggested material system becomes highly stiff and glassy, lowering the loss factors after a specific aspect ratio due to the mentioned phenomenon. However, regardless of the aspect ratio of the CNTs, it is easy to see that as the CNTs content increases, all loss factors improve. Experiments by de Borbón et al. [93] and micromechanical analysis by Finegan et al. [94] came to similar conclusions about the impacts of aspect ratio.

3.4.3 Effects of interfacial compliance (α_0) on the viscoelastic properties

Figure 12 shows the influence of non-dimensional interfacial compliance (α_0) and carbon nanotube content (v_{NC}^{CNT}) on the viscoelastic characteristics of hybrid nanocomposites. Figure 12a–d show that storage moduli fall as interfacial compliance (α_0) increases, which is understandable given the fact that when CNTs-polymer interfacial compliance increases in the NC phase, the material system becomes more flexible regardless of CNTs content (v_{NC}^{CNT}). Figure 12e–h show that as interfacial compliance (α_0) increases, all loss factors increase, regardless of CNTs content (v_{NC}^{CNT}). This is because increasing, α_0 promotes CNTs movement inside the polymer phase, which aids energy dissipation. At lower v_{NC}^{CNT}, the effect of interfacial compliance (α_0) on the viscoelastic property is more pronounced.

3.4.4 Effects of interfacial loss factor ($\alpha^{''}/\alpha^{'}$) on the viscoelastic properties

Figure 13 illustrates the relationship between the interfacial loss factor ($\alpha^{''}/\alpha\prime$) and the carbon nanotube content (v_{NC}^{CNT}) on the viscoelastic properties of multi-scale hybrid nanocomposites. The storage moduli depicted in Fig. 13a–d exhibit a notable decrease as $\alpha^{''}/\alpha\prime$ increases. This decline suggests that the interfacial storage modulus plays a crucial role in rendering the multiscale composite flexible and leathery (or rubbery), irrespective of v_{NC}^{CNT}. Moreover, as the v_{NC}^{CNT} increases, the influence of $\alpha^{''}/\alpha\prime$ on the storage moduli becomes more pronounced.

In Fig. 13e–h, it is evident that all loss factors exhibit an ascendant trend with an increase in interfacial loss factor ($\alpha^{''}/\alpha\prime$), regardless of nanotube content (v_{NC}^{CNT}). This trend is attributed to the simultaneous rise in both interfacial and overall damping properties of the proposed multiscale hybrid composite material system. Essentially, as the interfacial

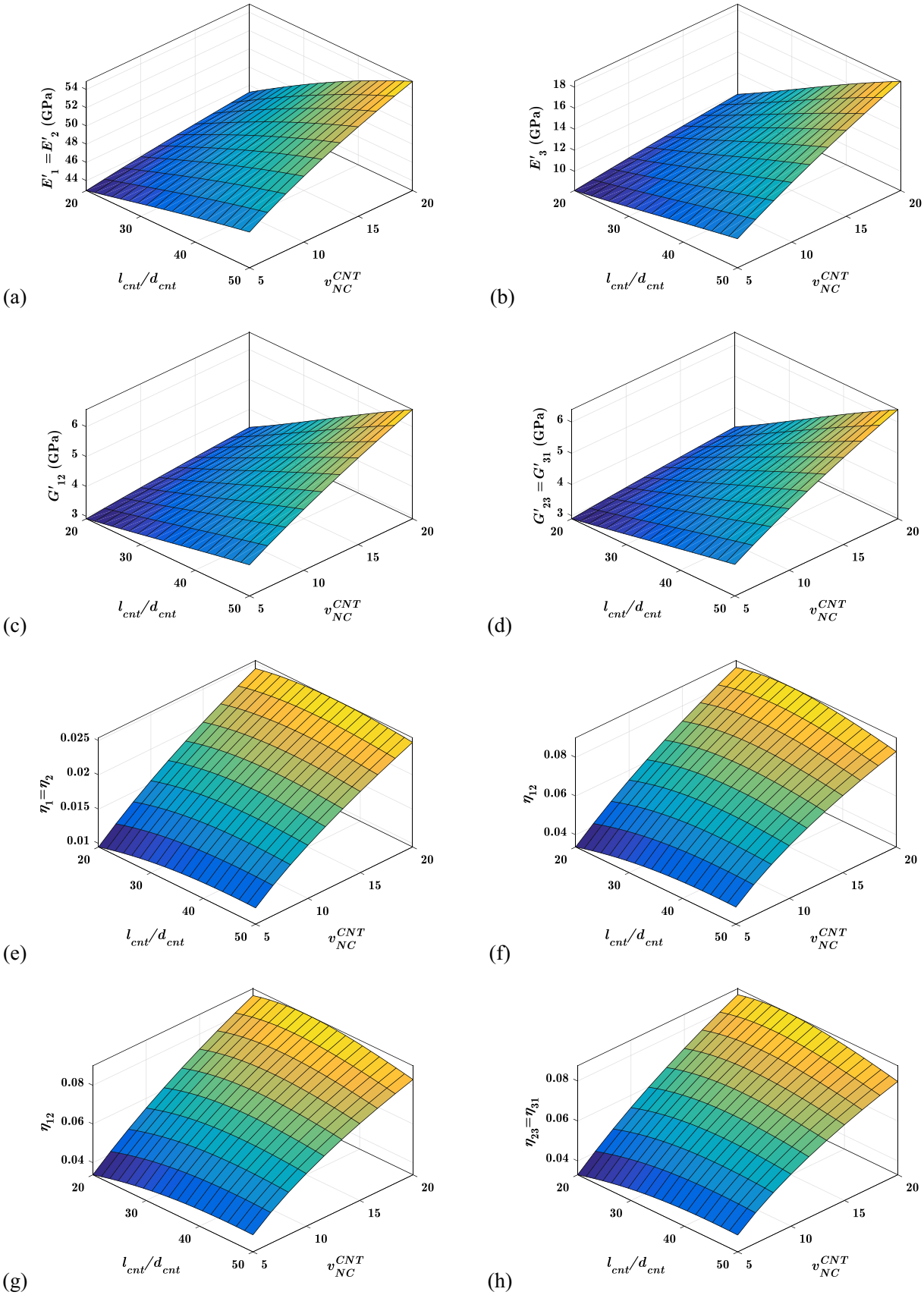

Fig. 11 Variation of the viscoelastic properties with v_{NC}^{CNT} and l_{cnt}/d_{cnt}

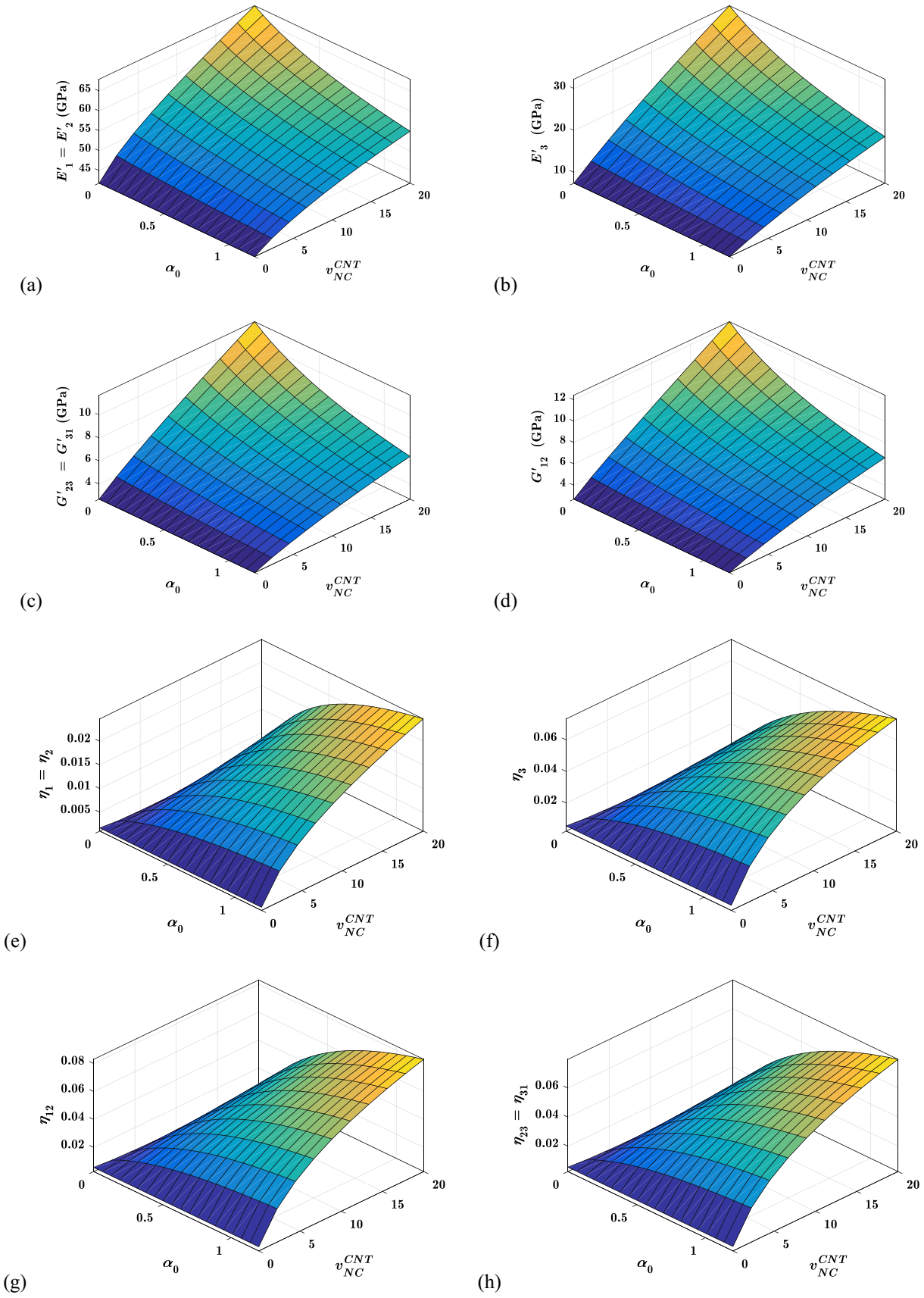

Fig. 12 Variation of the viscoelastic properties with α_0 and v_{NC}^{CNT}

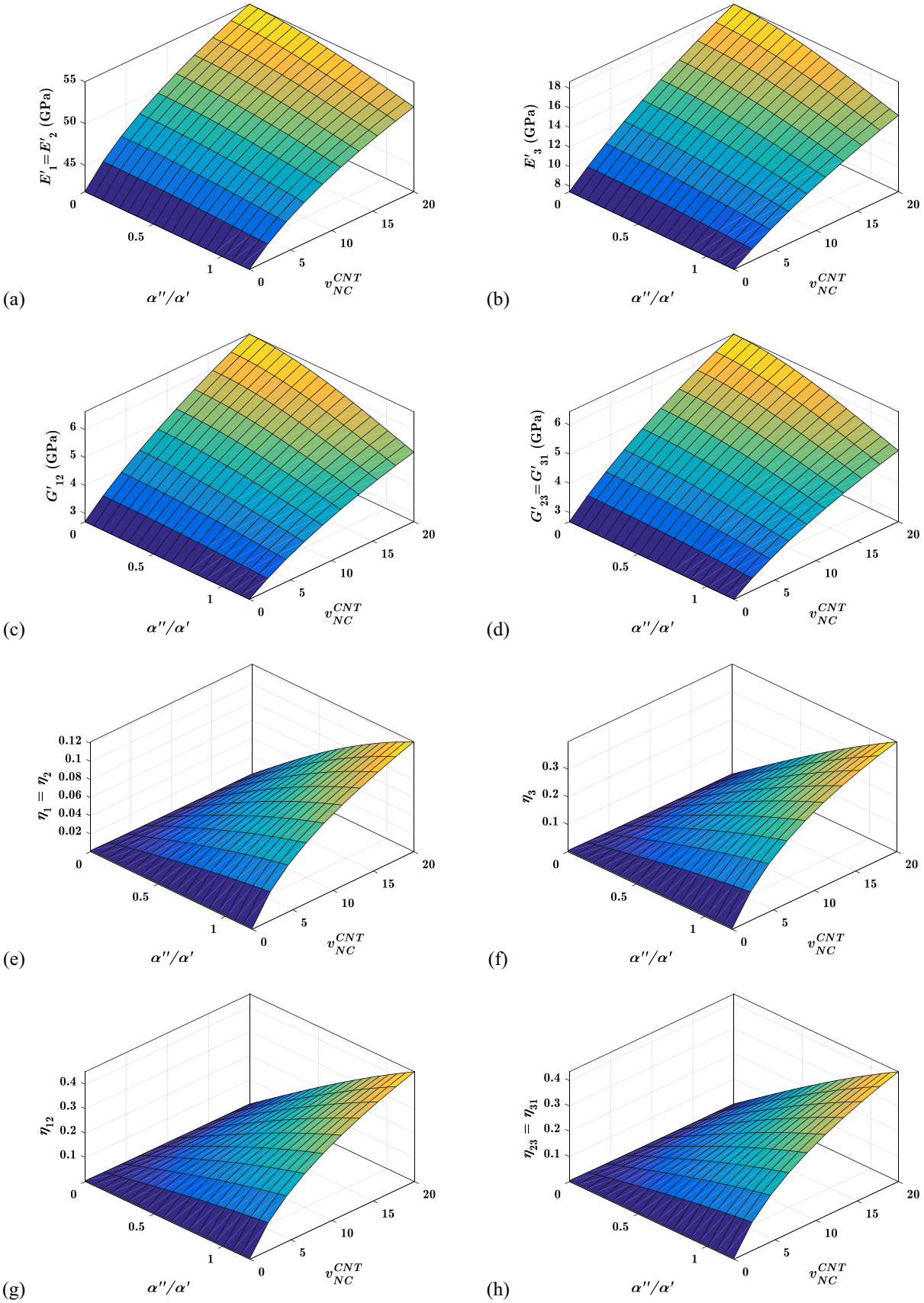

Fig. 13 Variation of the viscoelastic properties with $\alpha^{''}/\alpha'$ and v_{NC}^{CNT}

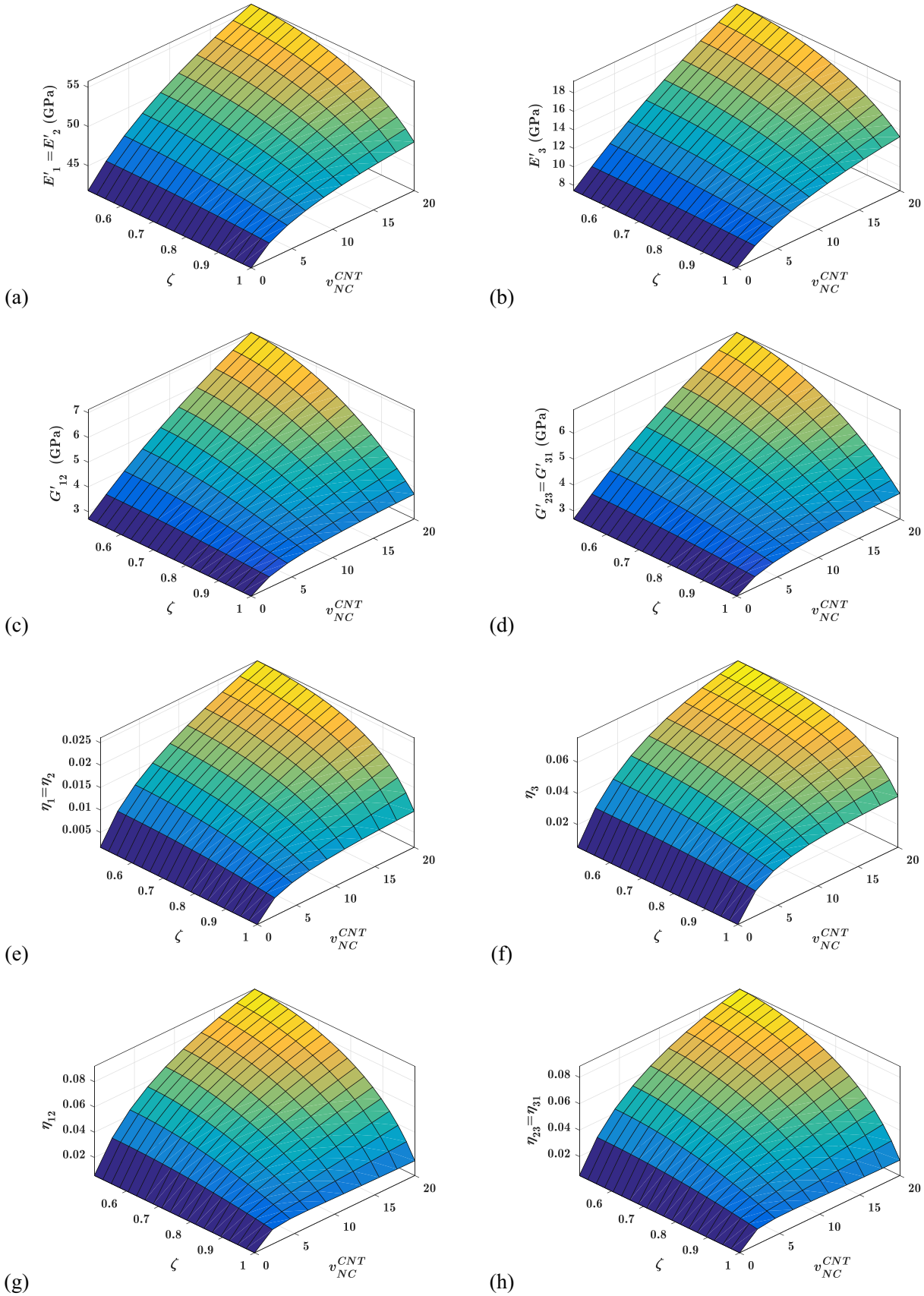

Fig. 14 Variation of the viscoelastic properties with ζ and v_{NC}^{CNT}

damping property increases, it contributes to an overall increase in the damping capability of the hybrid composite material. This observation emphasizes the significant role of interfacial interactions between polymer and carbon nanotube in dictating the viscoelastic behaviour of nanocomposite materials.

3.4.5 Effects of agglomeration parameter (ζ)on the viscoelastic properties

The viscoelastic characteristics of the proposed woven fabric hybrid nanocomposite for various agglomeration parameters (ζ) and CNTs content (v_{NC}^{CNT}) are shown in Fig. 14. Figure 14 shows that as the agglomeration parameter (ζ) is increased, all of the storage moduli and loss factors degrade. Figure 14 further shows that as v_{NC}^{CNT} increases, the influence of ζ on storage moduli and loss factors increases. After approximately 5%, v_{NC}^{CNT} becomes ineffective in terms of improving all loss moduli at a higher value of ζ. As $\zeta = V_{cluster}^{CNT}/V^{CNT}$, a rise in ζ will ensure an increase in the volume of CNTs in the cluster. CNTs outside the cluster diminish as the number of CNTs or volume of CNTs in the cluster grows. The volume outside the cluster is substantial, and the population of CNTs is significantly lower than the population of CNTs within the cluster. Because the volume of inclusions is so relatively small in relation to the volume outside of the inclusion in an RVE, the material property outside the cluster always dominates the viscoelastic characteristics of the proposed hybrid composite. As a result, increasing ζ deteriorates both elastic and damping properties.

3.4.6 Effects of agglomeration parameter (ξ) on the viscoelastic properties

The viscoelastic properties of the proposed hybrid woven-fabric nanocomposite material for various agglomeration parameters (ξ) and CNTs contents (v_{NC}^{CNT}) are shown in Fig. 15. Figure 15 shows that increasing ξ improves all storage moduli and loss factors of the proposed material system. By definition, $\xi = V^{cluster}/V^{NC}$ (i.e. the volume fraction of the cluster with respect to the nanocomposite) so the volume of clusters inside the nanocomposite grows as ξ increases. Because this cluster may be thought of as a reinforcing phase in the material system, increasing ξ will increase the volume of clusters with respect to the nanocomposite. So increase in ξ enhances the storage and loss factor of the inclusion. As a result, the NC's overall attributes have improved.

3.4.7 Effects of temperature (T) and excitation frequency (ω) on the viscoelastic properties

Figure 16 shows the changes in viscoelastic properties of proposed material systems as a function of temperature (T) and excitation frequency (ω). Figure 16 illustrates that temperature and excitation frequency have a considerable impact on the viscoelastic properties of the said material system. All the storage moduli increases as the excitation frequency (ω) increase, as seen in Fig. 16a–d. According to the matrix property, the loss factors vary with excitation frequency, as shown in Fig. 16e–h. This means that the hybrid composite can act glassy and rubbery at a given frequency regardless of temperature. The proposed composite material systems have lower storage moduli and larger loss moduli at higher temperatures, as shown in Fig. 16, as at lower temperatures, the polymer is more glassy.

3.4.8 Effects of the thickness of the yarn (t_f) and width of yarn ($S_{Ff}t_f$) on the viscoelastic properties

Figure 17 represents the viscoelastic properties of the proposed woven fabric hybrid nanocomposite for the various width of yarn ($S_{Ff}t_f$) and thickness of the yarn (t_f). Figure 17a, b demonstrate the variations of the volume fraction of fibre in *RUC* (v_{RUC}^{NCF}) and crimp angle (β_{cf}) with respect to fill-yarn thickness (t_f) and width of fill yarn ($S_{Ff}t_f$). Figure 17a shows that when the yarn thickness (t_f) increase, so does the value of v_{RUC}^{NCF}. for the lower value of yarn width ($S_{Ff}t_f$) how ever at higher levels of yarn width ($S_{Ff}t_f$) there is no substantial fluctuation in v_{RUC}^{NCF} with regard to yarn thickness (t_f). These effets are seen as yarn thickness (t_f) increases the volume fraction of *NCF* phase in the *RUC* for a certain breadth of yarn ($S_{Ff}t_f$). In the instance of crimp angle (β_{cf}) variations as illustrated in Fig. 17b, it can be seen that the crimp angle (β_{cf}) increase as yarn thickness (t_f) increases; on the other hand, it reduces with the increase in yarn width ($S_{Ff}t_f$). When the section e-f-g-h in Fig. 6 is taken into consideration, the crimp angle (β_{cf}) increases as the yarn thickness (t_f) increases. However,

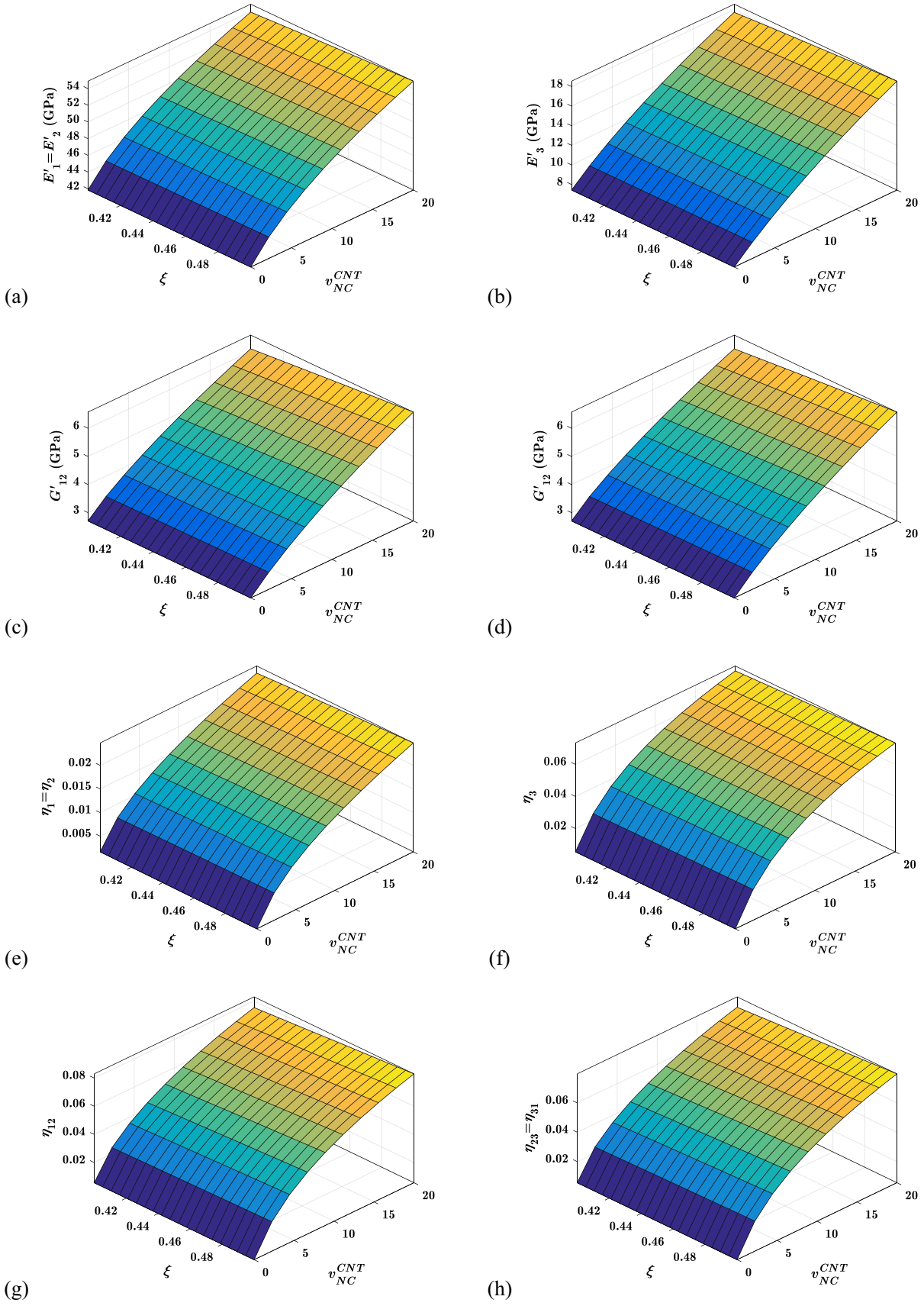

Fig. 15 Variation of the viscoelastic properties with ξ and v_{NC}^{CNT}

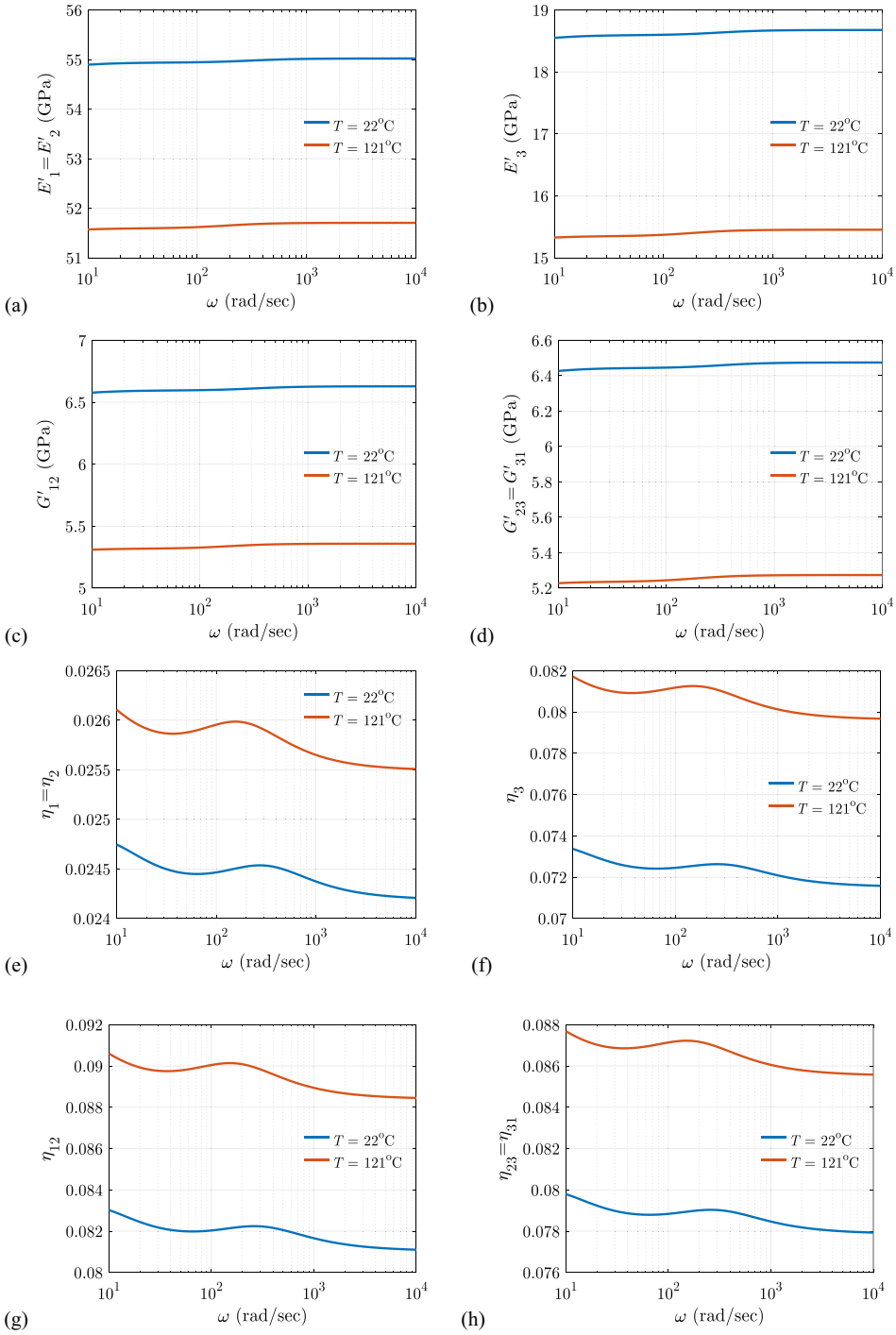

Fig. 16 Variation of the viscoelastic properties with T and ω

when sections a-b-c-d and e-f-g-h, as illustrated in Fig. 6, are considered, it can be ascertained that for a fixed thickness of yarn (t_f), increasing the width of the yarn ($S_{Ff}t_f$) will result in a decrease in crimp angle.

Figure 17c shows the variation of in-pane storage modulus ($E_1\prime$) with respect to yarn thickness (t_f) and yarn width ($S_{Ff}t_f$). It is clear that the in-pane storage modulus ($E_1\prime$) improves as the yarn width ($S_{Ff}t_f$) increases. However, irrespective of the value of yarn width ($S_{Ff}t_f$), the in-pane storage modulus ($E_1\prime$) deteriorates with yarn thickness (t_f). As a result, it can be stated that increasing yarn thickness (t_f) has almost no effect on the in-pane storage modulus ($E_1\prime$) however, it can be stated that the width of the yarn ($S_{Ff}t_f$) significantly improves the in-pane storage modulus ($E_1\prime$). The fluctuation of the in-plane loss factor (η_1) in Fig. 17d demonstrates that it follows the trend of crimp angle (β_{cf}). It means with the

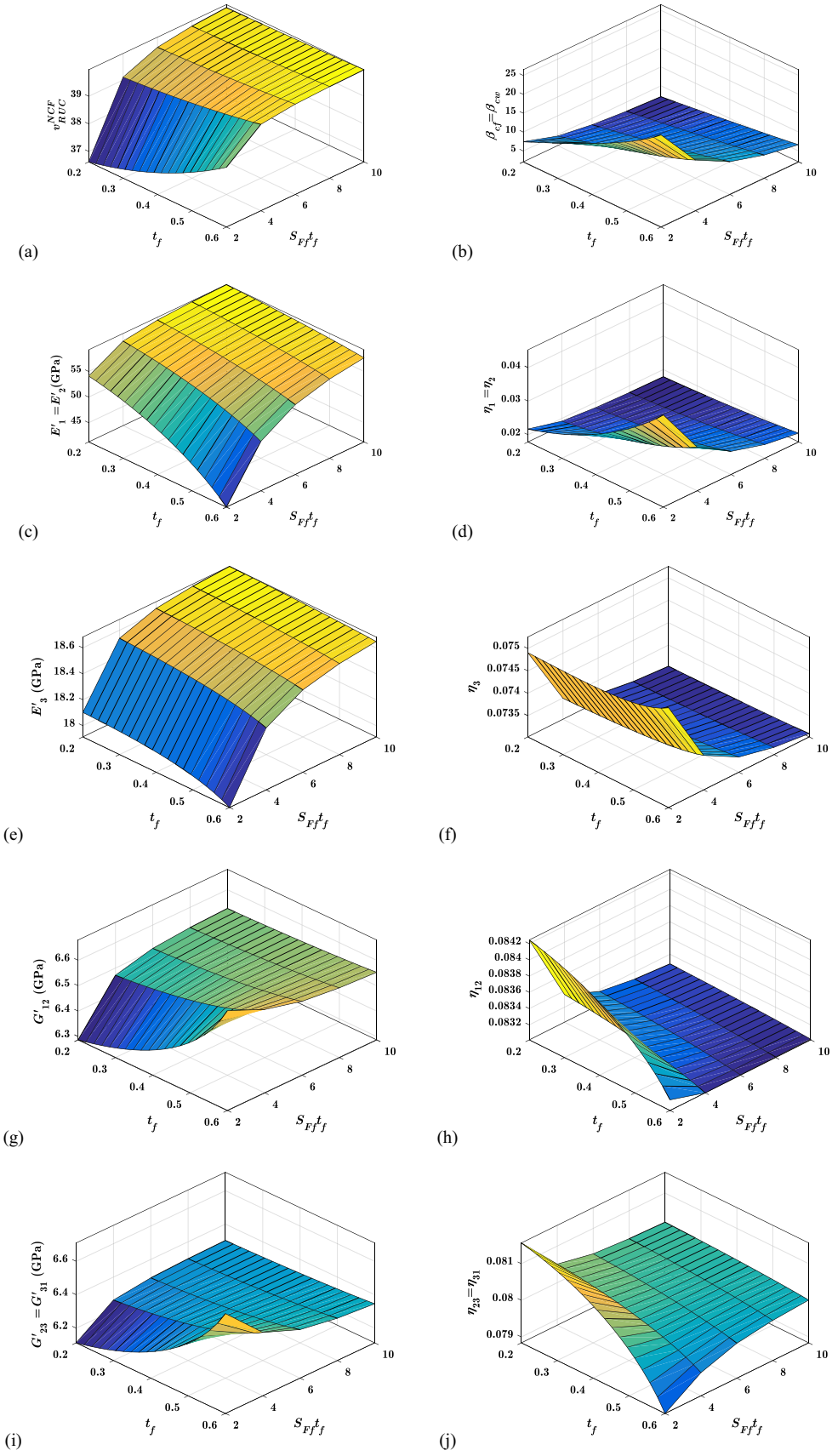

Fig. 17 Variation of the viscoelastic properties with $S_{Ff}t_f$ and t_f

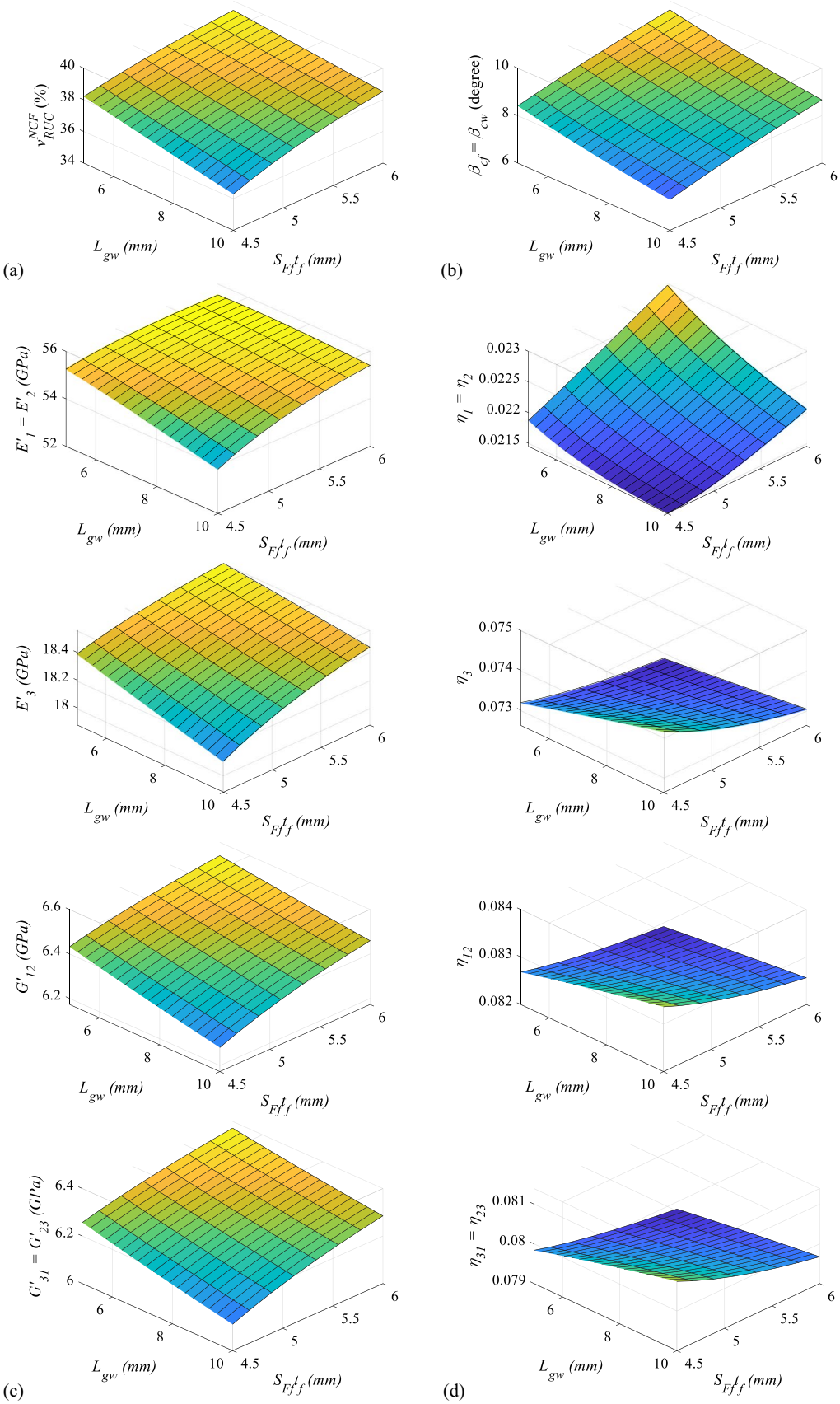

Fig. 18 Variation of the viscoelastic properties with L_{gw} and $S_{Ff}t_f$

increase in crimp angle (β_{cf}) the proposed hybrid nanocomposite material system behaves as more rubbery or leathery when it is stretched (or compressed) periodically in direction 1 (or 2)

The variation of out–of–plane storage modulus ($E_3\prime$) with yarn thickness (t_f) and yarn width ($S_{Ff}t_f$) is shown in Fig. 17e. It is evident from Fig. 17c, e that the out–of–plane storage modulus ($E_3\prime$) has a trend similar to that of in-pane storage modulus ($E_1\prime$) which means the width of the yarn ($S_{Ff}t_f$) significantly influences out–of–plane storage modulus ($E_3\prime$) than the yarn thickness (t_f). In Fig. 17f, the variation of the out-of-plane loss factor (η_3) shows that when yarn width ($S_{Ff}t_f$) increases out-of-plane loss factor (η_3) degrades. The variation in yarn thickness (t_f) has a negligible effect on the out-of-plane loss factor (η_3).

Variations of in-plane shear storage modulus ($G_{12}\prime$) in Fig. 17g and out-of-plane shear storage modulus ($G_{23}\prime$) in Fig. 17i indicate that they both improve with yarn width ($S_{Ff}t_f$) at lower values of yarn thickness (t_f) but these properties ($G_{12}\prime$ and $G_{23}\prime$) deteriorate with yarn thickness ($S_{Ff}t_f$) at higher values of yarn thickness (t_f). Figure 17h shows the variation of in-plane shear loss factor (η_{12}) which suggests that the yarn width ($S_{Ff}t_f$) and yarn thickness (t_f) deteriorates the in-plane shear loss factor (η_{12}) which means the proposed hybrid nanocomposite system will behave more glassy when it is cyclically excited in shear mode 1–2. Out-of-plane shear loss factor (η_{23}) in Fig. 17j depicts that for a higher value of yarn thickness (t_f), out-of-plane shear loss factor (η_{23}) improves with an increase in yarn width ($S_{Ff}t_f$).

3.4.9 Effects of the gap between two yarns on the viscoelastic properties

Variation of viscoelastic properties of proposed multiscale woven fabric hybrid nanocomposite for various gap (L_{gw}) and yarn width ($S_{Ff}t_f$) are shown in Fig. 18, where Fig. 18a, b demonstrate the change in the volume fraction of fibre in *RUC* (v_{RUC}^{NCF}) and yarn crimp angle (β_{cf}) with regard to gap (L_{gw}) and yarn width ($S_{Ff}t_f$). Figure 18a shows that v_{RUC}^{NCF} decreases with gap (L_{gw}) regardless of yarn width ($S_{Ff}t_f$). Figure 18a shows that when the width of the yarn ($S_{Ff}t_f$) increase, v_{RUC}^{NCF} improves as well, irrespective of the value of gap (L_{gw}). Similarly, the change of crimp angle (β_{cf}) in Fig. 18b clarifies that it reduces with the increase of gap (L_{gw}), irrespective of the value of width if the yarn ($S_{Ff}t_f$) which can also be realized when section e-f-g-h in Fig. 6 is analyzed.

Figure 18c shows the variation of in-plane and out-of-plane storage moduli ($E_1\prime$, $E_3\prime$, $G_{12}\prime$, and $G_{23}\prime$) with respect to gap (L_{gw}) and yarn width ($S_{Ff}t_f$). It can be depicted from Fig. 18c that all these properties decrease with an increase in the gap (L_{gw}) however, increase with an increase in yarn width ($S_{Ff}t_f$). The gap (L_{gw}) reduces v_{RUC}^{NCF} which causes a reduction in the storage moduli (viz. $E_1\prime$, $E_3\prime$, $G_{12}\prime$, and $G_{23}\prime$). In-pane loss factors (η_1) is deteriorating with the gap (L_{gw}) whereas other loss factors (viz. η_3, η_{12}, and η_{23}) in Fig. 18d indicates that all of them improves with gap (L_{gw}) irrespective of the yarn width ($S_{Ff}t_f$) suggesting that these loss factors (η_3, η_{12}, and η_{23}) have an inverse trend to that of v_{RUC}^{NCF}

3.4.10 Effects of dissimilar yarns thickness on the viscoelastic properties

In order to study the effect of dissimilar yarn thickness on the viscoelastic properties, the thickness of warp yarn (t_w) is varied, keeping the thickness of the fill yarn constant to assess the viscoelastic property of the multi-scale composite material system. Figure 19a depicts the variation of the volume fraction of fibre in *RUC* (v_{RUC}^{NCF}) and yarn crimp angles (β_{cf} and β_{cw}) with regard to yarn thickness (t_f). It can be observed that both the fraction of fibre (v_{RUC}^{NCF}) and crimp angles (β_{cf} and β_{cw}) increase with the increase in thickness (t_w), which is quite apparent. It is further observed that the effect of warp thickness (t_w) on fill yarn crimp angle (β_{cf}) is more than that of warp yarn crimp angle (β_{cw}). Again, the trend of volume fraction of fibre in *RUC* (v_{RUC}^{NCF}) has more semblance to the trend of fill yarn crimp angle (β_{cf}). Figure 19b depicts the variation of longitudinal ($E_1\prime$ and $E_2\prime$) and transverse ($E_3\prime$) storage modulus with thickness (t_w). It is worth noticing that the $E_1\prime$ Increase with an increase of t_w. On the other hand, t_w has a negative impact on $E_2\prime$ until $t_w < t_f$. Warp yarn thickness does not affect transverse ($E_3\prime$) storage modulus. Figure 19c focuses on the variation of longitudinal (η_1 and η_2) and transverse loss factors (η_3) with thickness (t_w). It can be observed from the figure that the longitudinal loss factor (η_1) decrease with an increase in warp yarn thickness (t_w). On the other hand, the longitudinal loss factor η_2 increase with the increase in warp yarn thickness (t_w) until $t_w < t_f$. The transverse loss factor (η_3) is uninfluenced with warp yarn thickness (t_w). As depicted in Fig. 19d, all the shear storage moduli ($G_{12}\prime$, $G_{13}\prime$ and $G_{23}\prime$) improve with an increase in warp yarn thickness (t_w) whereas Fig. 19e, suggests that shear loss factors η_{12}, and η_{23} deteriorate with an increase in warp yarn thickness (t_w) whereas η_{13} show slight improvement with warp yarn thickness (t_w). It is worth mentioning that the variation in the thickness of warp and fill yarn will result in making the material system anisotropic.

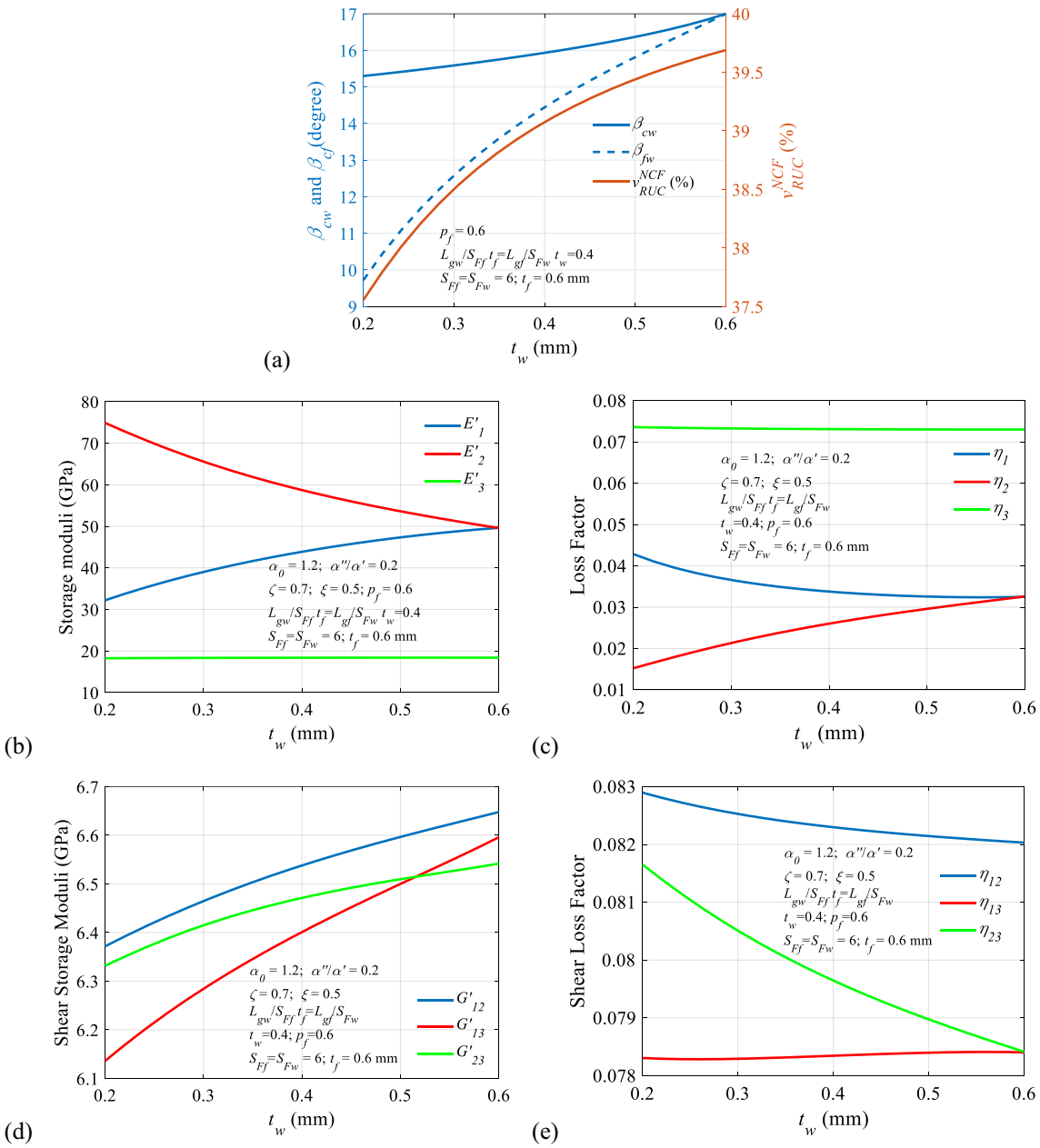

Fig. 19 Variation of the viscoelastic properties with t_f

4 Performance evaluation test

In order to evaluate the performance of the proposed composite, a finite element based vibration test has been conducted on spherical laminate with the stacking sequence of $[0/-45/45/90]_{2s}$ and simply supported boundary conditions as taken in Ref. [95, 96] after proper validation and convergence study of the shell finite element formulations (Ref. [66, 97]) as implemented by Swain and Roy [66]. A shell described here is the most versatile structural element that can consider such material properties. The versatility of the shell is such that it can approximate a plate with a higher radius of curvature. It can behave as a beam if one edge is comparatively smaller than another. To highlight the versatility of the micromechanics and for brevity, only one type of geometry of the shell panel with only simply supported boundary condition is considered in this study. The required matrices used for the performance evaluation study are also mentioned in Appendix E. In the current performance evaluation v_{NC}^{CNT} is varied as 0%, 10% and 20% keeping all the parameters constants as shown in Frequency responses plot in Fig. 20. It is evident from Fig. 20 as v_{NC}^{CNT} is increased, the absolute

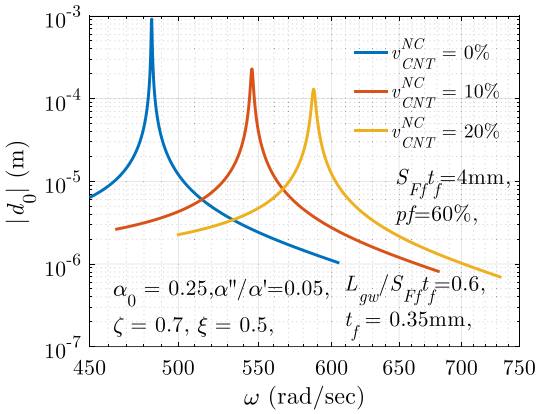

Fig. 20 Frequency responses of the proposed hybrid spherical shell panel (R/a =10 and a/h =100) for various v_{NC}^{CNT}

Table 4 Comparison of first natural frequency and loss factor for shell panel with R/a =10 and a/h =100

Parameters		ω_1	η_1
v_{NC}^{CNT} (% age)	0	484.39	08.574×10^{-04}
	10	545.71	27.918×10^{-04}
	20	587.26	42.196×10^{-04}

amplitude of the shell mid-surface ($|d_0|$) is decreased, whereas the resonant frequency is shifted to higher values desired for a wide range of applications. The results of the modal analysis of such shell panels are shown in Table 4. It is depicted from Table 4 that the first natural frequency and the first modal loss factors also improved due to in collusion of CNTs in the polymer phase. It is clear that the CNTs have improved the natural frequency by 12.66% and 21.24% and modal loss factors by 255.61% and 392.14% by increasing of v_{NC}^{CNT} by 10% and 20% respectively. The impulse response shown in Fig. 21 shows a similar implication of improving the damping of the spherical shell panel. It is evident from the figure that the response of the panel with the highest CNTs content damps more effectively when compared to shell panels with lesser CNTs content.

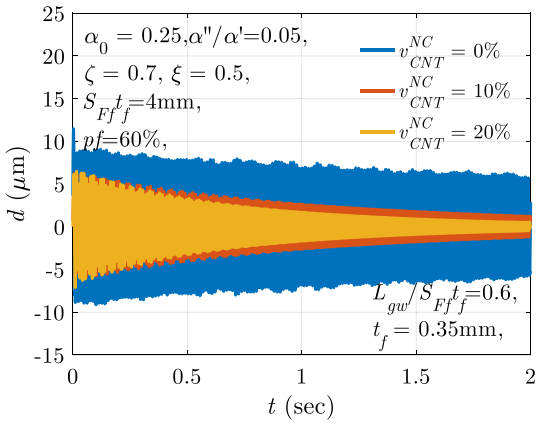

Fig. 21 Impulse responses of the proposed hybrid spherical shell panel (R/a =10 and a/h =100) for various v_{NC}^{CNT}

5 Conclusions

This study introduces a novel micromechanical framework for evaluating the viscoelastic properties of a two-dimensional (2D) woven hybrid composite reinforced with multiscale carbon nanotubes (CNTs). Initially, a comprehensive description of the constructional features of the 2D woven trans-scale composite material system is provided. The mathematical modeling of the material properties of each constituent phase or building block is established to evaluate the homogenized viscoelastic properties of the proposed composite material system based on the nature of the constructional feature. In order to emphasize the originality of this research, the viscoelastic properties of the modified matrix are evaluated by using the Tanaka (MT) micromechanics method in conjunction with the weak viscoelastic interphase (WI) theory. The CNTs are assumed to be randomly orientated inside the polymer phase. The mathematical frameworks for the viscoelastic features of yarns are established using the strength of the material (SOM) approach. In contrast, the viscoelastic properties of the representative unit cell (RUC) are determined using the unit cell method (UCM). Variations in the carbon nanotube (CNT) content, interface conditions, agglomeration, carbon fiber volume fraction, excitation frequency, and temperature have yielded diverse numerical outcomes. This study also investigates the impact of geometrical characteristics, such as yarn thickness, breadth, and gap length, on the viscoelasticity of composite material systems. The study has shown that not only all the storage moduli but also all the material loss factors improved with CNT content. On the other hand, the aggregation deteriorated the storage modulus. The result suggests that the deterioration of all the storage and loss factors is significant at higher CNT content. Again, it is also verified that the aspect ratio of CNT helps improve the storage modulus. However, the loss factors improved first with the aspect ratio and became unaffected by a further increase in the aspect ratio. The weak interphase deteriorated the storage modulus but improved the loss factors. The yarn geometry is essential in determining the viscoelastic property of the material system. It is observed that the yarn thickness has negatively impacted the longitudinal and transverse storage modulus but improved all the shear storage modulus. All the loss factors except the out-of-plane shear loss factor declined with increased yarn width. Out-of-plane shear loss factor showed a mixed trend; at a lower value of yarn thickness, it deteriorated and improved at a higher value of yarn thickness. Gap has a negative effect on all the storage and inplane loss factors. On the other hand, out-of-plane loss factors and all shear loss factors improved with gap length. The present investigation also examines the matter of anisotropic viscoelastic properties that arise as a consequence of employing yarns of unequal thicknesses. The findings of this micromechanical research offer significant insights into the viscoelastic characteristics of the proposed composite material system and indicate its potential utility in the field of vibration damping. In order to showcase the practical implementation of newly developed micromechanics in the analysis of vibration, a significant contribution is made by comprehensive numerical experiments on a shell panel. In the frequency response and transient response analysis, the findings indicate a notable decrease in vibration amplitudes when compared to conventional composite materials. In order to prioritize the examination of micromechanical behavior in connection to dynamic response, this study exclusively considers linear strain displacement relationships for brevity. These observations have the potential to guide future investigations and advancements in the realm of composite materials. Numerical performance study reveals that these multiscale hybrid composites can be used in the application of vibration reduction.

Author contributions AS: Conceptualization, Methodology, Investigation, Software, Validation, Original draft preparation, Writing—review & editing, Supervision; TR: Methodology, Investigation, Visualization, Supervision; SF:Validation, Data curation, Writing- Original draft preparation; VP: Validation, Data curation, Writing- Original draft preparation; BT: Visualization, Writing- Writing—review & Editing, Original draft preparation.

Funding None.

Data availability The authors declare that the data supporting the findings of this study are available within the paper.

Declarations

Competing interests The authors declare that they have no known competing financial interests or personal relationships that could have appeared to influence the work reported in this paper.

Appendix A

Eshelby's tensor is given by [98]

$$S_{ijkl} = \frac{1}{8\pi} C^{P}_{pqmn}\left(G_{ipjq} + G_{jpiq}\right) \tag{A1}$$

$$G_{1111} = \frac{\pi}{2}\int_0^1 \Delta\left(1-x^2\right)\left[\left\{\hat{f}\left(1-x^2\right)+\hat{h}\hat{\rho}^2x^2\right\}\left\{\left(3\hat{e}+\hat{d}\right)\left(1-x^2\right)+4\hat{f}\hat{\rho}^2x^2\right\}-\hat{g}^2\hat{\rho}^2x^2\left(1-x^2\right)\right]dx$$

$$G_{1122} = \frac{\pi}{2}\int_0^1 \Delta\left(1-x^2\right)\left[\left\{\hat{f}\left(1-x^2\right)+\hat{h}\hat{\rho}^2x^2\right\}\left\{\left(\hat{e}+3\hat{d}\right)\left(1-x^2\right)+4\hat{f}\hat{\rho}^2x^2\right\}-3\hat{g}^2\hat{\rho}^2x^2\left(1-x^2\right)\right]dx$$

$$G_{1133} = 2\pi\int_0^1 \Delta\hat{\rho}^2x^2\left[\left\{\left(\hat{d}+\hat{e}\right)\left(1-x^2\right)+2\hat{f}\hat{\rho}^2x^2\right\}\left\{\hat{f}\left(1-x^2\right)+\hat{h}\hat{\rho}^2x^2\right\}-\hat{g}^2\hat{\rho}^2x^2\left(1-x^2\right)\right]dx$$

$$G_{1212} = \frac{\pi}{2}\int_0^1 \Delta\left(1-x^2\right)^2\left[\hat{g}^2\hat{\rho}^2x^2-\left(\hat{d}-\hat{e}\right)\left\{\hat{f}\left(1-x^2\right)+\hat{h}\hat{\rho}^2x^2\right\}\right]dx$$

$$G_{1313} = 2\pi\int_0^1 \Delta\hat{g}\hat{\rho}^2x^2\left(1-x^2\right)\left\{\hat{e}\left(1-x^2\right)+\hat{f}\hat{\rho}^2x^2\right\}dx$$

$$G_{3311} = 2\pi\int_0^1 \Delta\left(1-x^2\right)\left\{\hat{d}\left(1-x^2\right)+\hat{f}\hat{\rho}^2x^2\right\}\left\{\hat{e}\left(1-x^2\right)+\hat{f}\hat{\rho}^2x^2\right\}dx$$

$$G_{3333} = 4\pi\int_0^1 \Delta\hat{\rho}^2x^2\left\{\hat{d}\left(1-x^2\right)+\hat{f}\hat{\rho}^2x^2\right\}\left\{\hat{e}\left(1-x^2\right)+\hat{f}\hat{\rho}^2x^2\right\}dx$$

$$G_{2222} = G_{1111}$$

$$G_{2211} = G_{1122}$$

$$G_{2233} = G_{1133}$$

$$G_{3322} = G_{3311}$$

$$G_{2323} = G_{1313}$$

and

$$\hat{d} = C^{P}_{1111}$$

$$\widehat{e}=\frac{C^P_{1111}-C^P_{1122}}{2}$$

$$\widehat{f}=C^P_{2323}$$

$$\widehat{g}=C^P_{1133}+C^P_{2323}$$

$$\widehat{h}=C^P_{3333}$$

$$\widehat{\rho}=\frac{1}{\widehat{\alpha}}$$

$$\Delta^{-1}=\left\{\widehat{e}\left(1-x^2\right)+\widehat{f}\widehat{\rho}^2x^2\right\}\left[\left\{\widehat{d}\left(1-x^2\right)+\widehat{f}\widehat{\rho}^2x^2\right\}\left\{\widehat{f}\left(1-x^2\right)+\widehat{h}\widehat{\rho}^2x^2\right\}-\widehat{g}^2\widehat{\rho}^2x^2\left(1-x^2\right)\right]$$

For $\widehat{\alpha}=\infty$, an explicit expressions for the nonzero element of the Eshelby's tensor reported by Li and Dunn [99] are.

$$S_{1111}=S_{2222}=\frac{5C^P_{1111}+C^P_{1122}}{8C^P_{1111}}$$

$$S_{1122}=S_{2211}=\frac{3C^P_{1122}-C^P_{1111}}{8C^P_{1111}}$$

$$S_{1212}=S_{1221}=S_{2112}=S_{2121}=\frac{3C^P_{1111}-C^P_{1122}}{8C^P_{1111}}$$

$$S_{1133}=S_{2233}=\frac{C^P_{1133}}{2C^P_{1111}}$$

$$S_{2323}=S_{2332}=S_{3223}=S_{3232}=S_{1313}=S_{1331}=S_{3113}=\frac{1}{4}$$

Appendix B

Parameters associated with weak interface

$$P_{ijkl}=\frac{3}{16\pi}\int_0^{\pi}\left[\int_0^{2\pi}\frac{\delta_{ik}\widehat{n}_j\widehat{n}_l+\delta_{jk}\widehat{n}_i\widehat{n}_l+\delta_{il}\widehat{n}_k\widehat{n}_j+\delta_{jl}\widehat{n}_k\widehat{n}_i}{n}d\theta\right]\sin\phi d\phi \tag{B1}$$

$$Q_{ijkl}=\frac{3}{4\pi}\int_0^{\pi}\left[\int_0^{2\pi}\frac{\widehat{n}_i\widehat{n}_j\widehat{n}_k\widehat{n}_l}{n^3}d\theta\right]\sin\phi d\phi \tag{B2}$$

$$n=\sqrt{\widehat{n}_i\widehat{n}_i}$$

$$\widehat{n}_i = \left(\frac{\sin\phi\cos\theta}{a_1} \quad \frac{\sin\phi\sin\theta}{a_2} \quad \frac{\cos\phi}{a_3} \right)^T$$

For cylindrical inclusions $a_1 = a_2 = a$ and $a_3 \to \infty$. Hence equation above reduces to.

$$P_{1111} = P_{2222} = 4P_{2323} = 4P_{1313} = 2P_{1212} = \frac{3\pi}{8a}$$

$$Q_{1111} = Q_{2222} = 3Q_{1122} = 3Q_{2211} = 3Q_{1212} = \frac{9\pi}{32a}$$

With other terms being zeros.

Appendix C

$$[V_1] = \left[[V_3] + [V_4][C_4]^{-1}[C_3] \right]^{-1} [V_2] = \left[[V_4] + [V_3][C_3]^{-1}[C_4] \right]^{-1}; \tag{C1}$$

$$[C_1] = v_{NCF}^F \begin{bmatrix} c_{11}^F & c_{12}^F & c_{13}^F & 0 & 0 & 0 \\ 0 & 0 & 0 & 0 & 0 & 0 \\ 0 & 0 & 0 & 0 & 0 & 0 \\ 0 & 0 & 0 & 0 & 0 & 0 \\ 0 & 0 & 0 & 0 & 0 & 0 \\ 0 & 0 & 0 & 0 & 0 & 0 \end{bmatrix} \tag{C2}$$

$$[C_2] = \begin{bmatrix} v_{NCF}^{NC} c_{11}^{NC} & v_{NCF}^{NC} c_{12}^{NC} & v_{NCF}^{NC} c_{13}^{NC} & 0 & 0 & 0 \\ c_{12}^{NC} & c_{22}^{NC} & c_{23}^{NC} & 0 & 0 & 0 \\ c_{13}^{NC} & c_{23}^{NC} & c_{33}^{NC} & 0 & 0 & 0 \\ 0 & 0 & 0 & c_{44}^{NC} & 0 & 0 \\ 0 & 0 & 0 & 0 & c_{55}^{NC} & 0 \\ 0 & 0 & 0 & 0 & 0 & c_{66}^{NC} \end{bmatrix}; \tag{C3}$$

$$[V_3] = \begin{bmatrix} 0 & 0 & 0 & 0 & 0 & 0 \\ 0 & v_{NCF}^F & 0 & 0 & 0 & 0 \\ 0 & 0 & v_{NCF}^F & 0 & 0 & 0 \\ 0 & 0 & 0 & v_{NCF}^F & 0 & 0 \\ 0 & 0 & 0 & 0 & v_{NCF}^F & 0 \\ 0 & 0 & 0 & 0 & 0 & v_{NCF}^F \end{bmatrix}; \tag{C4}$$

$$[V_4] = \begin{bmatrix} 1 & 0 & 0 & 0 & 0 & 0 \\ 0 & v_{NCF}^{NC} & 0 & 0 & 0 & 0 \\ 0 & 0 & v_{NCF}^{NC} & 0 & 0 & 0 \\ 0 & 0 & 0 & v_{NCF}^{NC} & 0 & 0 \\ 0 & 0 & 0 & 0 & v_{NCF}^{NC} & 0 \\ 0 & 0 & 0 & 0 & 0 & v_{NCF}^{NC} \end{bmatrix}; \tag{C4}$$

$$[C_3] = \begin{bmatrix} 1 & 0 & 0 & 0 & 0 & 0 \\ c_{12}^F & c_{22}^F & c_{23}^F & 0 & 0 & 0 \\ c_{13}^F & c_{23}^F & c_{33}^F & 0 & 0 & 0 \\ 0 & 0 & 0 & c_{44}^F & 0 & 0 \\ 0 & 0 & 0 & 0 & c_{55}^F & 0 \\ 0 & 0 & 0 & 0 & 0 & c_{66}^F \end{bmatrix};$$

$$[C_4] = \begin{bmatrix} 1 & 0 & 0 & 0 & 0 & 0 \\ c_{12}^{NC} & c_{22}^{NC} & c_{23}^{NC} & 0 & 0 & 0 \\ c_{13}^{NC} & c_{23}^{NC} & c_{33}^{NC} & 0 & 0 & 0 \\ 0 & 0 & 0 & c_{44}^{NC} & 0 & 0 \\ 0 & 0 & 0 & 0 & c_{55}^{NC} & 0 \\ 0 & 0 & 0 & 0 & 0 & c_{66}^{NC} \end{bmatrix} \tag{C5}$$

Appendix D

$$\begin{aligned} &A_{\bar{w}} = \frac{3\beta_{cw}}{8} + \frac{\sin\left(2\beta_{cw}\right)}{4} + \frac{\sin\left(4\beta_{cw}\right)}{32}; \quad B_{\bar{w}} = \frac{3\beta_{cw}}{8} - \frac{\sin\left(2\beta_{cw}\right)}{4} + \frac{\sin\left(4\beta_{cw}\right)}{32} \\ &C_{\bar{w}} = \frac{\beta_{cw}}{8} - \frac{\sin\left(4\beta_{cw}\right)}{32}; \quad D_{\bar{w}} = \frac{\beta_{cw}}{2} + \frac{\sin\left(2\beta_{cw}\right)}{4}; \quad E_{\bar{w}} = \frac{\beta_{cw}}{2} - \frac{\sin\left(2\beta_{cw}\right)}{4} \\ &F_{\bar{w}} = \frac{\cos^4\left(\beta_{cw}\right)}{2} - \frac{1}{2}; \quad G_{\bar{w}} = \left(\cos^2\left(\beta_{cw}\right) - 1\right)^2; \quad H_{\bar{w}} = \frac{F_{\bar{w}}}{2} + \frac{G_{\bar{w}}}{4} \\ &I_{\bar{w}} = \frac{\sin^2\left(\beta_{cw}\right)}{2}; \quad J_{\bar{w}} = \frac{\beta_{cw}}{2} - \frac{\sin\left(4\beta_{cw}\right)}{8}; \quad K_{\bar{w}} = \frac{\beta_{cw}}{2} + \frac{\sin\left(4\beta_{cw}\right)}{8} \end{aligned} \tag{D1}$$

Appendix E

The equation of motion can be expressed as follows:

$$\left[M_{uu}^e\right]\left\{\ddot{d}^e\right\} + \left[K_{uu}^e\right]\left\{d^e\right\} = \left\{f^e\right\} \tag{E1}$$

In its final form, the mass matrix can be stated as follows:

$$\left[M_{uu}^e\right] = \int_{-1}^{1}\int_{-1}^{1}\int_{-h/2}^{h/2} \rho[N]^T[N]dz|J|d\xi d\eta \tag{E2}$$

The matrix of element structural stiffness can be calculated as follows [97]:

$$\left[K_{uu}^e\right] = \int_V \left[B_u^e\right]^T[C]\left[B_u^e\right]dV \tag{E3}$$

$$\left[K_{uu}^e\right] = \left[K_{bb}^e\right] + \left[K_{ss}^e\right]$$

$$\left[B_u^e\right] = \begin{bmatrix} \left[B_b^e\right] & [0] \\ [0] & \left[B_s^e\right] \end{bmatrix}$$

$$[C] = \begin{bmatrix} [D_b] & [0] \\ [0] & [D_s] \end{bmatrix}$$

The element in a laminated composite structure's plane/bending stiffness matrix $\left[K_{bb}^e\right]$ can be calculated as follows.

$$\left[K_{bb}^e\right] = \int_V \left[B_b^e\right]^T [D_b] \left[B_b^e\right] dV = \int_\Omega \left[B_b^e\right]^T \begin{bmatrix} [A] & [B] \\ [B] & [D] \end{bmatrix} \left[B_b^e\right] d\Omega$$

The transverse shear stiffness matrix $\left[K_{ss}^e\right]$ of an element can be represented as follows:

$$\left[K_{ss}^e\right] = \int_\Omega \left[B_s^e\right]^T [D_s] \left[B_s^e\right] d\Omega$$

The element external force vector $\{f^e\}$ can be obtained if the external load is dispersed over the surface with a magnitude of f_s^e by using the relation:

$$\left\{f^e\right\} = \int_A [N]^T \left\{f_s^e(x,y)\right\} dA \tag{E4}$$

The strain displacement relation can be found by [95]

$$\left[B_b^e\right] = \sum \begin{bmatrix} \frac{\partial N_i}{\partial \alpha_1} & \frac{N_i}{A_1 A_2}\frac{\partial A_1}{\partial \alpha_2} & \frac{N_i}{R_1} & 0 & 0 \\ \frac{N_i}{A_1 A_2}\frac{\partial A_2}{\partial \alpha_1} & \frac{1}{A_2}\frac{\partial N_i}{\partial \alpha_2} & \frac{N_i}{R_2} & 0 & 0 \\ \frac{1}{A_2}\frac{\partial N_i}{\partial \alpha_2} - \frac{N_i}{A_1 A_2}\frac{\partial A_1}{\partial \alpha_2} & \frac{1}{A_1}\frac{\partial N_i}{\partial \alpha_1} - \frac{N_i}{A_1 A_2}\frac{\partial A_2}{\partial \alpha_1} & \frac{2N_i}{R_{12}} & 0 & 0 \\ -\frac{1}{2}\frac{1}{R_{12}}\left(\frac{1}{A_2}\frac{\partial N_i}{\partial \alpha_2} + \frac{N_i}{A_1 A_2}\frac{\partial A_1}{\partial \alpha_2}\right) & \frac{1}{2}\frac{1}{R_{12}}\left(\frac{1}{A_1}\frac{\partial N_i}{\partial \alpha_1} + \frac{N_i}{A_1 A_2}\frac{\partial A_2}{\partial \alpha_1}\right) & 0 & \frac{1}{A_1}\frac{\partial N_i}{\partial \alpha_1} & \frac{N_i}{A_1 A_2}\frac{\partial A_1}{\partial \alpha_2} \\ \frac{1}{2}\frac{1}{R_{12}}\left(\frac{1}{A_2}\frac{\partial N_i}{\partial \alpha_2} + \frac{N_i}{A_1 A_2}\frac{\partial A_1}{\partial \alpha_2}\right) & -\frac{1}{2}\frac{1}{R_{12}}\left(\frac{1}{A_1}\frac{\partial N_i}{\partial \alpha_1} + \frac{N_i}{A_1 A_2}\frac{\partial A_2}{\partial \alpha_1}\right) & 0 & \frac{N_i}{A_1 A_2}\frac{\partial A_2}{\partial \alpha_1} & \frac{1}{A_2}\frac{\partial N_i}{\partial \alpha_2} \\ C_0\left(\frac{1}{A_2}\frac{\partial N_i}{\partial \alpha_2} + \frac{N_i}{A_1 A_2}\frac{\partial A_1}{\partial \alpha_2}\right) & -C_0\left(\frac{1}{A_1}\frac{\partial N_i}{\partial \alpha_1} + \frac{N_i}{A_1 A_2}\frac{\partial A_2}{\partial \alpha_1}\right) & 0 & \frac{1}{A_2}\frac{\partial N_i}{\partial \alpha_2} - \frac{N_i}{A_1 A_2}\frac{\partial A_1}{\partial \alpha_2} & \frac{1}{A_1}\frac{\partial N_i}{\partial \alpha_1} - \frac{N_i}{A_1 A_2}\frac{\partial A_2}{\partial \alpha_1} \end{bmatrix} \tag{E5}$$

where, $C_0 = \frac{1}{2}\left(\frac{1}{R_1} - \frac{1}{R_2}\right)$

$$\left[B_s^e\right] = \sum \begin{bmatrix} -\frac{N_i}{R_{12}} & -\frac{N_i}{R_2} & \frac{1}{A_2}\frac{\partial N_i}{\partial \alpha_2} & 0 & N_i \\ -\frac{N_i}{R_1} & -\frac{N_i}{R_{12}} & \frac{1}{A_1}\frac{\partial N_i}{\partial \alpha_1} & N_i & 0 \end{bmatrix} \tag{E6}$$

where,

$$\begin{aligned} N_1 &= \tfrac{1}{4}(1-\xi)(1-\eta)(-1-\xi-\eta) \\ N_2 &= \tfrac{1}{2}(1-\xi^2)(1-\eta) \\ N_3 &= \tfrac{1}{4}(1+\xi)(1-\eta)(-1+\xi-\eta) \\ N_4 &= \tfrac{1}{2}(1+\xi)(1-\eta^2) \\ N_5 &= \tfrac{1}{4}(1+\xi)(1+\eta)(-1+\xi+\eta) \\ N_6 &= \tfrac{1}{2}(1-\xi^2)(1+\eta) \\ N_7 &= \tfrac{1}{4}(1-\xi)(1+\eta)(-1-\xi+\eta) \\ N_8 &= \tfrac{1}{2}(1-\xi)(1-\eta^2) \end{aligned}$$

$$[N] = \begin{bmatrix} N_1 & 0 & 0 & 0 & 0 & \dots & N_n & 0 & 0 & 0 & 0 \\ 0 & N_1 & 0 & 0 & 0 & \dots & 0 & N_n & 0 & 0 & 0 \\ 0 & 0 & N_1 & 0 & 0 & \dots & 0 & 0 & N_n & 0 & 0 \\ 0 & 0 & 0 & N_1 & 0 & \dots & 0 & 0 & 0 & N_n & 0 \\ 0 & 0 & 0 & 0 & N_1 & \dots & 0 & 0 & 0 & 0 & N_n \end{bmatrix} \tag{E7}$$

$$[C] = \begin{bmatrix} [D_b] & [0] \\ [0] & [D_s] \end{bmatrix} = \begin{bmatrix} A_{11} & A_{12} & A_{16} & B_{11} & B_{12} & B_{16} & 0 & 0 \\ A_{12} & A_{22} & A_{26} & B_{12} & B_{22} & B_{26} & 0 & 0 \\ A_{16} & A_{26} & A_{66} & B_{16} & B_{26} & B_{66} & 0 & 0 \\ B_{11} & B_{12} & B_{16} & D_{11} & D_{12} & D_{16} & 0 & 0 \\ B_{12} & B_{22} & B_{26} & D_{12} & D_{22} & D_{26} & 0 & 0 \\ B_{16} & B_{26} & B_{66} & D_{16} & D_{26} & D_{66} & 0 & 0 \\ 0 & 0 & 0 & 0 & 0 & 0 & A_{44} & A_{45} \\ 0 & 0 & 0 & 0 & 0 & 0 & A_{45} & A_{55} \end{bmatrix} \tag{E8}$$

$$\left(A_{ij} \;\; B_{ij} \;\; D_{ij} \right) = \int_{-\frac{h}{2}}^{+\frac{h}{2}} \left(1 \;\; z \;\; z^2 \right) \overline{Q_{ij}} \mathrm{dz}; \left(A_{ij}^{s} \right) = \int_{-\frac{h}{2}}^{+\frac{h}{2}} k_s \overline{Q_{ij}} \mathrm{dz} \tag{E9}$$

Open Access This article is licensed under a Creative Commons Attribution 4.0 International License, which permits use, sharing, adaptation, distribution and reproduction in any medium or format, as long as you give appropriate credit to the original author(s) and the source, provide a link to the Creative Commons licence, and indicate if changes were made. The images or other third party material in this article are included in the article's Creative Commons licence, unless indicated otherwise in a credit line to the material. If material is not included in the article's Creative Commons licence and your intended use is not permitted by statutory regulation or exceeds the permitted use, you will need to obtain permission directly from the copyright holder. To view a copy of this licence, visit http://creativecommons.org/licenses/by/4.0/.

References

1. Ishikawa T, Chou T-W. Elastic behavior of woven hybrid composites. J Compos Mater. 1982;16:2–19. https://doi.org/10.1177/002199838201600101.
2. Yang J-M, Ma C-L, Chou T-W. Fiber inclination model of three-dimensional textile structural composites. J Compos Mater. 1986;20:472–84. https://doi.org/10.1177/002199838602000505.
3. Zhang YC, Harding J. A numerical micromechanics analysis of the mechanical properties of a plain weave composite. Comput Struct. 1990;36:839–44.
4. Naik NK, Ganesh VK. Prediction of on-axes elastic properties of plain weave fabric composites. Compos Sci Technol. 1992;45:135–52.
5. Shembekar PS, Naik NK. Elastic behavior of woven fabric composites: II–laminate analysis. J Compos Mater. 1992;26:2226–46. https://doi.org/10.1177/002199839202601503.
6. Naik NK, Ganesh VK. Failure behavior of plain weave fabric laminates under on-axis uniaxial tensile loading: I—analytical predictions. J Compos Mater. 1996;30:1779–822. https://doi.org/10.1177/002199839603001603.
7. Ganesh VK, Naik NK. Failure behavior of plain weave fabric laminates under on-axis umnaxial tensile loading: III–effect of fabric geometry. J Compos Mater. 1996;30:1823–56. https://doi.org/10.1177/002199839603001604.
8. Vandeurzen P, Ivens J, Verpoest I. A three-dimensional micromechanical analysis of woven-fabric composites: I. Geometric analysis. Compos Sci Technol. 1996;56:1303–15.
9. Vandeurzen P, Ivens J, Verpoest I. A three-dimensional micromechanical analysis of woven-fabric composites: II. Elastic analysis. Compos Sci Technol. 1996;56:1317–27.
10. Scida D, Aboura Z, Benzeggagh ML, et al. A micromechanics model for 3D elasticity and failure of woven-fibre composite materials. Compos Sci Technol. 1999;59:505–17.
11. Barbero EJ, Damiani TM, Trovillion J. Micromechanics of fabric reinforced composites with periodic microstructure. Int J Solids Struct. 2005;42:2489–504.

12. Barbero EJ, Trovillion J, Mayugo JA, et al. Finite element modeling of plain weave fabrics from photomicrograph measurements. Compos Struct. 2006;73:41–52.
13. Donadon MV, Falzon BG, Iannucci L, et al. A 3-D micromechanical model for predicting the elastic behaviour of woven laminates. Compos Sci Technol. 2007;67:2467–77.
14. Naik NK, Shembekar PS. Elastic behavior of woven fabric composites: I-lamina analysis. J Compos Mater. 1992;26:2196–225. https://doi.org/10.1177/002199839202601502.
15. Barbero EJ. Introduction to composite materials design [Internet]. CRC Press; 2011.
16. Adumitroaie A, Barbero EJ. Stiffness and strength prediction for plain weave textile reinforced composites. Mech Adv Mater Struct. 2012;19:169–83. https://doi.org/10.1080/15376494.2011.572245.
17. Kowalczyk P. Parametric constitutive model of plain-weave fabric reinforced composite ply. Adv Compos Mater. 2016;25:287–303. https://doi.org/10.1080/09243046.2014.996959.
18. Shokrieh M, Ghasemi R, Mosalmani R. A general micromechanical model to predict elastic and strength properties of balanced plain weave fabric composites. J Compos Mater. 2017. https://doi.org/10.1177/0021998317716530?casa_token=Wrbn5cU22NkAAAAA%3ADxmhT9K8QILsiDlRirFxpgFRDGM_HdfNrNm8gzyw6cwEtTTvz6xzRKf7hXYXM4zN5_pYyjzCNA68qQ.
19. Wang J, Wen L, Xiao J, et al. The mechanical properties and constitutive model of two woven composites including the influences of temperature, strain rate and damage growth. Compos Part B Eng. 2019;161:502–13.
20. Hwang G, Kim DH, Kim M. Structure optimization of woven fabric composites for improvement of mechanical properties using a micro-mechanics model of woven fabric composites and a genetic algorithm. Compos Adv Mater. 2021;30:263498332110061. https://doi.org/10.1177/26349833211006114.
21. Scida D, Aboura Z, Benzeggagh ML, et al. Prediction of the elastic behaviour of hybrid and non-hybrid woven composites. Compos Sci Technol. 1998;57:1727–40.
22. Cheour K, Assarar M, Scida D, et al. Effect of water ageing on the mechanical and damping properties of flax-fibre reinforced composite materials. Compos Struct. 2016;152:259–66.
23. Govindarajan S, Langrana NA, Weng GJ. An experimental and theoretical study of creep of a graphite/epoxy woven composite. Polym Compos. 1996;17:353–61. https://doi.org/10.1002/pc.10621.
24. Ishikawa T, Chou T-W. Stiffness and strength behaviour of woven fabric composites. J Mater Sci. 1982;17:3211–20. https://doi.org/10.1007/BF01203485.
25. Zhu Q, Shrotriya P, Sottos NR, et al. Three-dimensional viscoelastic simulation of woven composite substrates for multilayer circuit boards. Compos Sci Technol. 2003;63:1971–83.
26. Rupnowski P, Kumosa M. Meso- and micro-stress analyses in an 8HS graphite/polyimide woven composite subjected to biaxial in-plane loads at room temperature. Compos Sci Technol. 2003;63:785–99.
27. Shrotriya P, Sottos NR. Creep and relaxation behavior of woven glass/epoxy substrates for multilayer circuit board applications. Polym Compos. 1998;19:567–78. https://doi.org/10.1002/pc.10130.
28. Shrotriya P, Sottos NR. Viscoelastic response of woven composite substrates. Compos Sci Technol. 2005;65:621–34.
29. Kim YK. Viscoelastic effect of FR-4 material on packaging stress development. IEEE Trans Adv Packag. 2007;30:411–20.
30. Sottos NR, Ockers JM, Swindeman M. Thermoelastic properties of plain weave composites for multilayer circuit board applications. J Electron Packag. 1999;121:37.
31. Greco A, Musardo C, Maffezzoli A. Flexural creep behaviour of PP matrix woven composite. Compos Sci Technol. 2007;67:1148–58.
32. Naik A, Abolfathi N, Karami G, et al. Micromechanical viscoelastic characterization of fibrous composites. J Compos Mater. 2008;42:1179–204. https://doi.org/10.1177/0021998308091221.
33. Upadhyaya P, Upadhyay CS. A three-dimensional micromechanical model to predict the viscoelastic behavior of woven composites. Compos Struct. 2011;93:2733–9.
34. Jia X, Xia Z, Gu B. Nonlinear numerical predictions of three-dimensional orthogonal woven composite under low-cycle tension using multiscale repeating unit cells. Int J Damage Mech. 2015;24:338–62. https://doi.org/10.1177/1056789514532667.
35. Wang L, Zhao B, Wu J, et al. Experimental and numerical investigation on mechanical behaviors of woven fabric composites under off-axial loading. Int J Mech Sci. 2018;141:157–67.
36. Chen YH, Aliabadi MH. Micromechanical modelling of the overall response of plain woven polymer matrix composites. Int J Eng Sci. 2019;145:103163.
37. Bhattacharjee A, Ganguly K, Roy H. An operator based novel micromechanical model of viscoelastic hybrid woven fibre-particulate reinforced polymer composites. Eur J Mech A/Solids. 2020;83:104044.
38. Liu X, Peng B, Yu W. Multiscale modeling of the effective thermal conductivity of 2D woven composites by mechanics of structure genome and neural networks. Int J Heat Mass Transf. 2021;179:121673.
39. Wu L, Adam L, Noels L. Micro-mechanics and data-driven based reduced order models for multi-scale analyses of woven composites. Compos Struct. 2021;270:114058.
40. Bai J, Wang Z, Sobey A, et al. Micromechanical model for rapid prediction of plain weave fabric composite strengths under biaxial tension. Compos Struct. 2021;255:112888.
41. Joshi P, Upadhyay S. Effect of interphase on elastic behavior of multiwalled carbon nanotube reinforced composite. Comput Mater Sci. 2014;87:267–73.
42. Odegard GM, Gates TS, Wise KE, et al. Constitutive modeling of nanotube–reinforced polymer composites. Compos Sci Technol. 2003;63:1671–87.
43. Odegard GM, Clancy TC, Gates TS. Modeling of the mechanical properties of nanoparticle/polymer composites. Polymer (Guildf). 2005;46:553–62.
44. Zhang JG. The effect of carbon fibers and carbon nanotubes on the mechanical properties of polyimide composites. Mech Compos Mater. 2011;47:447–50. https://doi.org/10.1007/s11029-011-9222-x.
45. Dong C. Mechanical and thermo-mechanical properties of carbon nanotube reinforced composites. Int J Smart Nano Mater. 2014;5:44–58. https://doi.org/10.1080/19475411.2014.896427.

46. Khan MR, Mahfuz H, Adnan A, et al. Elastic properties of UHMWPE-SWCNT nanocomposites' fiber: an experimental, theoretic, and molecular dynamics evaluation. J Mater Eng Perform. 2013;22:1593–600. https://doi.org/10.1007/s11665-013-0471-9.
47. Kim M. Modeling, manufacturing, and characterization of nanocomposites and multiscale composites. UK: Florida State University; 2009.
48. Sadeghi M, Pol MH. Investigation of behaviors of glass/epoxy laminate composites reinforced with carbon nanotubes under quasi-static punch shear loading. J Sandw Struct Mater. 2019;21:1535–56. https://doi.org/10.1177/1099636217719223?casa_token=x1vbEzZNLogAAAAA%3AphxMq-sZq_MGpBrGWqEHITsccMu4ACkPtyJCIBo48AsZfTR6XuE1BHQrZEWrSH8GFnx_vB_RYslFig.
49. Dikshit V, Joshi SC. Modeling fiber bridging and matrix strengthening effect in multiscale-woven composites. In: Fiber-Reinforced Nanocomposites: Fundamentals and Applications. UK: Elsevier; 2020. p. 69–89.
50. Nam Y-W, Shin J-H, Choi J-H, et al. Micro-mechanical failure prediction of radar-absorbing structure dispersed with multi-walled carbon nanotubes considering multi-scale modeling. J Compos Mater. 2018;52:1649–60. https://doi.org/10.1177/0021998317729003.
51. Swain A, Baad S, Roy T. Modeling and analyses of thermo-elastic properties of radially grown carbon nanotubes-based woven fabric hybrid composite materials. Mech Adv Mater Struct. 2017;24:1206–20.
52. El Moumen A, Tarfaoui M, Lafdi K. Computational homogenization of mechanical properties for laminate composites reinforced with thin film made of carbon nanotubes. Appl Compos Mater. 2017;25:569–88. https://doi.org/10.1007/s10443-017-9636-2.
53. Fantuzzi N, Bacciocchi M, Agnelli J, et al. Three-phase homogenization procedure for woven fabric composites reinforced by carbon nanotubes in thermal environment. Compos Struct. 2020;254:112840.
54. Bilisik K, Syduzzaman M. Carbon nanotubes in carbon/epoxy multiscale textile preform composites: a review. Polym Compos. 2021;42:1670–97. https://doi.org/10.1002/pc.25955.
55. Guo A, Li S, Wang S, et al. Digital light processing of multi-walled carbon nanotubes-reinforced photosensitive resin composites: effects on microstructures and mechanical properties. J Mater Res Technol. 2024;28:434–45.
56. Wang S, Li S, Zhai Z, et al. Vibration characteristics of composite damping plate with randomly oriented carbon nanotube reinforced stiffeners. Int J Mech Mater Des. 2023
57. Huang X, Hao H, Oslub K, et al. Dynamic stability/instability simulation of the rotary size-dependent functionally graded microsystem. Eng Comput. 2022;38:4163–79.
58. Li J, Tang F, Habibi M. Bi-directional thermal buckling and resonance frequency characteristics of a GNP-reinforced composite nanostructure. Eng Comput. 2022;38:1559–80.
59. Al-Furjan MSH, Habibi M, Safarpour H. Vibration control of a smart shell reinforced by graphene nanoplatelets. Int J Appl Mech. 2020;12:2050066.
60. Al-Furjan MSH, Habibi M, Jung DW, et al. Chaotic responses and nonlinear dynamics of the graphene nanoplatelets reinforced doubly-curved panel. Eur J Mech A/Solids. 2021;85:104091.
61. Liu H, Shen S, Oslub K, et al. Amplitude motion and frequency simulation of a composite viscoelastic microsystem within modified couple stress elasticity. Eng Comput. 2022;38:3977–91.
62. Mohammadgholiha M, Shokrgozar A, Habibi M, et al. Buckling and frequency analysis of the nonlocal strain–stress gradient shell reinforced with graphene nanoplatelet. J Vib Control. 2019;25:2627–40.
63. Zheng W, Liu J, Oyarhossein MA, et al. Prediction of nth-order derivatives for vibration responses of a sandwich shell composed of a magnetorheological core and composite face layers. Eng Anal Bound Elem. 2023;146:170–83.
64. Lori ES, Ebrahimi F, Supeni EEB, et al. The critical voltage of a GPL-reinforced composite microdisk covered with piezoelectric layer. Eng Comput. 2021;37:3489–508.
65. Dai Z, Zhang L, Bolandi SY, et al. On the vibrations of the non-polynomial viscoelastic composite open-type shell under residual stresses. Compos Struct. 2021;263:113599.
66. Swain A, Roy T. Viscoelastic modelling and dynamic characteristics of CNTs-CFRP-2DWF composite shell structures. Compos Part B Eng. 2018;141:100–22.
67. Mori T, Tanaka K. Average stress in matrix and average elastic energy of materials with misfitting inclusions. Acta Metall. 1973;21:571–4.
68. Tanaka K, Wakashima K, Mori T. Plastic deformation anisotropy and work-hardening of composite materials. J Mech Phys Solids. 1973;21:207–14.
69. Weng GJ. Some elastic properties of reinforced solids, with special reference to isotropic ones containing spherical inclusions. Int J Eng Sci. 1984;22:845–56.
70. Benveniste Y. A new approach to the application of Mori-Tanaka's theory in composite materials. Mech Mater. 1987;6:147–57.
71. Qiu YP, Weng GJ. On the application of Mori-Tanaka's theory involving transversely isotropic spheroidal inclusions. Int J Eng Sci. 1990;28:1121–37.
72. Tucker CL III, Liang E. Stiffness predictions for unidirectional short-fiber composites: review and evaluation. Compos Sci Technol. 1999;59:655–71.
73. Schjødt-Thomsen J, Pyrz R. The Mori-Tanaka stiffness tensor: diagonal symmetry, complex fibre orientations and non-dilute volume fractions. Mech Mater. 2001;33:531–44.
74. Wang J, Pyrz R. Prediction of the overall moduli of layered silicate-reinforced nanocomposites—part I: basic theory and formulas. Compos Sci Technol. 2004;64:925–34.
75. Shi D-L, Feng X-Q, Huang YY, et al. The effect of nanotube waviness and agglomeration on the elastic property of carbon nanotube-reinforced composites. J Eng Mater Technol. 2004;126:250.
76. Esteva M, Spanos P. Effective elastic properties of nanotube reinforced composites with slightly weakened interfaces. J Mech Mater Struct. 2009;4:887–900.
77. Jiang B, Liu C, Zhang C, et al. Maximum nanotube volume fraction and its effect on overall elastic properties of nanotube-reinforced composites. Compos Part B Eng. 2009;40:212–7.
78. Meguid SA, Wernik JM, Cheng ZQ. Atomistic-based continuum representation of the effective properties of nano-reinforced epoxies. Int J Solids Struct. 2010;47:1723–36.
79. Seidel GD, Lagoudas DC. Micromechanical analysis of the effective elastic properties of carbon nanotube reinforced composites. Mech Mater. 2006;38:884–907.

80. Eshelby JD. The determination of the elastic field of an ellipsoidal inclusion, and related problems. Proc R Soc A Math Phys Eng Sci. 1957;241:376–96. https://doi.org/10.1098/rspa.1957.0133.
81. Qu J. The effect of slightly weakened interfaces on the overall elastic properties of composite materials. Mech Mater. 1993;14:269–81.
82. Sun LZ, Ju JW. Elastoplastic modeling of metal matrix composites containing randomly located and oriented spheroidal particles. J Appl Mech. 2004;71:774–85.
83. Swain A, Roy T. Viscoelastic modeling and vibration damping characteristics of hybrid CNTs-CFRP composite shell structures. Acta Mech. 2018;229:1321–52. https://doi.org/10.1007/s00707-017-2051-9.
84. Swain A, Roy T. Viscoelastic material damping characteristics of carbon nanotubes based functionally graded composite shell structures. Proc Inst Mech Eng Part L J Mater Des Appl. 2019;233:1510–41. https://doi.org/10.1177/1464420718764513?journalCode=pila.
85. Li R, Sun L. A micromechanics-based viscoelastic model for nanocomposites with imperfect interface. Int J Damage Mech. 2013;22:967–81. https://doi.org/10.1177/1056789512469890.
86. Lee S-K, Byun J-H, Hong SH. Effect of fiber geometry on the elastic constants of the plain woven fabric reinforced aluminum matrix composites. Mater Sci Eng A. 2003;347:346–58.
87. Li K, Gao X-L, Roy AK. Micromechanical modeling of viscoelastic properties of carbon nanotube-reinforced polymer composites. Mech Adv Mater Struct. 2006;13:317–28. https://doi.org/10.1080/15376490600583931.
88. Tornabene F, Fantuzzi N, Bacciocchi M, et al. Effect of agglomeration on the natural frequencies of functionally graded carbon nanotube-reinforced laminated composite doubly-curved shells. Compos Part B Eng. 2016;89:187–218.
89. Ashrafi B, Hubert P, Vengallatore S. Carbon nanotube-reinforced composites as structural materials for microactuators in microelectromechanical systems. Nanotechnology. 2006;17:4895–903.
90. Shen L, Li J. Transversely isotropic elastic properties of single-walled carbon nanotubes. Phys Rev B. 2004;69:045414. https://doi.org/10.1103/PhysRevB.69.045414.
91. Shen L, Li J. Erratum: transversely isotropic elastic properties of single-walled carbon nanotubes. Phys Rev B. 2010;81:119902. https://doi.org/10.1103/PhysRevB.81.119902.
92. Torayca. T300 Data Sheet [Internet]. No. CFA-001. 2002. p. 6–7. Available from: www.toraycfa.com/pdfs/T300DataSheet.pdf.
93. de Borbón F, Ambrosini D, Curadelli O. Damping response of composites beams with carbon nanotubes. Compos Part B Eng. 2014;60:106–10.
94. Finegan IC, Tibbetts GG, Gibson RF. Modeling and characterization of damping in carbon nanofiber/polypropylene composites. Compos Sci Technol. 2003;63:1629–35.
95. Swain A, Roy T, Nanda BK. Vibration damping characteristics of carbon nanotubes-based thin hybrid composite spherical shell structures. Mech Adv Mater Struct. 2017;24:95–113. https://doi.org/10.1080/15376494.2015.1107669.
96. Sk L, Sinha PK. Improved finite element analysis of multilayered, doubly curved composite shells. J Reinf Plast Compos. 2005;24:385–404. https://doi.org/10.1177/0731684405044899.
97. Swain A. Viscoelastic Modelling and Dynamic Analysis of CNT-based Composite Shell Panels, PhD thesis [Internet]. National Institute of Technology, Rourkela; 2018 [cited 2021 Dec 29]. Available from: http://ethesis.nitrkl.ac.in/9433/.
98. Mura T. Anisotropic inclusions. Micromechanics of defects in solids. Dordrecht: Springer; 1982. p. 110–49.
99. Li JY, Dunn ML. Anisotropic coupled-field inclusion and inhomogeneity problems. Philos Mag A. 1998;77:1341–50. https://doi.org/10.1080/01418619808214256.

Publisher's Note Springer Nature remains neutral with regard to jurisdictional claims in published maps and institutional affiliations.